An informative frequency band identification framework for gearbox fault diagnosis under time-varying operating conditions

Stephan Schmidt[a,*], P. Stephan Heyns[a], Konstantinos C. Gryllias[b,c]

[a] *Centre for Asset Integrity Management, Department of Mechanical and Aeronautical Engineering, University of Pretoria, Pretoria, South Africa*
[b] *Department of Mechanical Engineering, KU Leuven, Celestijnenlaan 300, 3001 Heverlee, Belgium*
[c] *Dynamics of Mechanical and Mechatronic Systems, Flanders Make, Belgium*

Abstract

The application of informative frequency band identification methods makes it possible to enhance weak damage components in the vibration signals acquired from rotating machines. Some rotating machines (e.g. wind turbines) operate inherently under time-varying operating conditions, however, very few frequency band identification methods have been developed with varying operating conditions in mind. Therefore, in this work, a systematic framework for obtaining consistent feature planes under time-varying operating conditions is proposed. This framework utilises the angle-frequency instantaneous power spectrum and the order-frequency cyclic modulation spectrum to construct feature planes. The kurtogram, the sparsogram, the infogram, the ICS2gram and the log-cycligram are obtained on numerical and experimental datasets acquired under time-varying operating conditions using this framework. In addition to this, we also implement the Informative Frequency Band Identification method using targeted cyclic orders, abbreviated to IFBI$_\alpha$gram, in this framework and compare the performance of this method against the other frequency band identification methods. Ultimately, we found that the feature used in the construction of the IFBI$_\alpha$gram is very well-suited for gear and bearing fault diagnosis under time-varying operating conditions.

Keywords:

Vibration-based condition monitoring, Time-varying operating conditions, Frequency band identification, IFBI$_\alpha$gram

*Corresponding author.
Email address: stephan.schmidt@up.ac.za (Stephan Schmidt)

1. Introduction

Condition monitoring forms an essential part of predictive maintenance programmes [1, 2] and has been a very active research field for gearboxes and bearings the past few decades [3–6]. This is due to the fact that gearboxes, which consist of bearings and gears, are critical subsystems in machines such as helicopters [7, 8], bucket wheel excavators [9] and wind turbines [10–13] and there usually are serious consequences and long downtimes associated with their failures [7, 14].

Vibration-based condition monitoring, which uses vibration data to infer the condition of the machine, is very popular for rotating machines, because it contains much information related to the condition of the gearbox. Machine learning [15, 16], deep learning [17–19] and signal processing methods [20, 21] have been developed to solve this problem. The measured vibration signals are typically contaminated by strong deterministic components [22–24], non-Gaussian noise [25] and time-varying operating conditions [9, 10, 26], which impede the ability to perform effective fault diagnosis. It is very important to find signal processing and analysis techniques that are capable of enhancing the signal or extracting the diagnostic information from the signal under such time-varying operating conditions.

Typically, synchronous averaging methods [26, 27], time-frequency methods and related techniques [12, 28–30], as well as squared envelope spectra [23] are used in the fault diagnosis process. It is possible to enhance the signal by applying Cepstrum-Pre Whitening (CPW) [24]; subtracting the generalised synchronous average from the signal [22, 23]; applying vibrational or stochastic resonance [31, 32]; designing matched and deconvolution filters [6, 33, 34]; or identifying informative frequency bands with Frequency Band Identification (FBI) methods [35–38]. FBI methods such as the kurtogram and the kurtosis-based methods [11, 33, 35, 39–42], the sparsogram [43], the infogram [44, 45], the autogram [46], the IESFOgram [47, 48], the IFBI$_\alpha$gram [49], the distcsgram [50], the ICS2gram [36], the log-cycligram [36] and the accugram [51] have been successfully used for rotating machine fault diagnosis. These methods have also been used as an integral part of more extensive methodologies to perform gearbox diagnostics [27, 52–54]. Smith et al. [36] made a distinction between blind methods and targeted FBI methods; targeted methods such as the ICS2gram and IFBI$_\alpha$gram target specific cyclic frequency content (e.g. characteristic

fault frequencies), while blind methods such as the kurtogram and sparsogram do not use any information related to the kinematics of the machine for FBI. However, many of the aforementioned methods have only been used under constant or quasi-stationary operating conditions or were specifically developed with constant or quasi-stationary operating conditions in mind. Critical rotating machines such as wind turbines operate inherently under time-varying operating conditions [10, 12] and therefore it is essential to find informative frequency band methods that are well-suited for varying operating conditions [36, 49].

The angular periodic impacts from damaged mechanical components (e.g. bearing damage) manifest in time-invariant frequency bands [55, 56], which have been used as basis for developing angle-time cyclostationary theory [55–58]. This means that conventional FBI methods, using time-frequency Short-Time Fourier Transform (STFT) and wavelet packet estimators to construct feature planes, do not necessarily preserve the fault information. This could adversely affect the performance of frequency band identification methods, especially targeted methods, under time-varying operating conditions and therefore a framework for identifying informative frequency bands is necessary.

The Angle-Frequency Instantaneous Power Spectrum (AF-IPS) and the Order-Frequency Cyclic Modulation Spectrum (OFCMS) provide a representation that preserves the angle-time properties of vibration signals acquired under time-varying speed conditions [12, 56]. In Ref. [56], a thorough analysis of the statistical properties of the OFCMS is performed and the OFCMS is used for damage detection under time-varying speed conditions. By combining the conventional FBI methods with the AF-IPS and OFCMS, it would be possible to perform FBI under time-varying operating conditions. Therefore, we develop a framework that utilises the recently published AF-IPS and OFCMS [56] for frequency band identification under time-varying operating conditions.

In summary, the following contributions are made with this work:

- A framework is proposed for identifying informative frequency bands under time-varying operating conditions.
- Different conventional frequency band identification methods, implemented using this method, are compared in this work under time-varying operating conditions.

This makes it possible to compare the performance of different features for frequency band identification under time-varying operating conditions, e.g. the kurtosis feature can be compared against the feature used in the original IFBI$_\alpha$gram [49].

- The IFBI$_\alpha$gram is implemented with this framework and it is compared to the order-frequency spectral coherence-based IFBI$_\alpha$gram used in Ref. [49].

The layout of the paper is as follows: An overview of the proposed frequency band identification framework is presented in Section 2 and an overview of different features is given, including the new IFBI$_\alpha$gram. Thereafter, the performance of the different features are compared in Section 3 on numerical gearbox data that simulate distributed gear damage, inner race bearing damage and outer race bearing damage. Lastly, the different features are compared on two experimental datasets that were acquired under time-varying operating conditions in Section 4, whereafter conclusions are drawn in Section 5. Lastly, Appendix A contains additional information pertaining to the numerical gearbox model.

2. Frequency Band Identification under time-varying operating conditions

The objective of the Frequency Band Identification (FBI) problem is to identify a frequency band $[f - \Delta f/2, f + \Delta f/2]$ in a signal $\boldsymbol{x} = [x[0], x[1], \dots x[N_x - 1]]$, with a length of N_x and sampled at a rate of f_s Hz, which would improve the signal-to-noise ratio of the characteristic-of-interest (e.g. improve the detectability of the damage). The bandpass filtered signal

$$\boldsymbol{x}_f = [x[0; f, \Delta f], x[1; f, \Delta f], \dots, x[N_x - 1; f, \Delta f]], \tag{1}$$

can then be analysed for damage with techniques such as the Squared Envelope Spectrum (SES) and the synchronous average of the squared envelope [27, 59].

The frequency band of interest $[f - \Delta f/2, f + \Delta f/2]$ can be determined by calculating a metric, a health index, or a feature, denoted by Ψ, of the bandlimited signal $\boldsymbol{x}_f$ for each potential combination of candidate centre frequencies f and bandwidths Δf, whereafter the band is selected by maximising the feature, i.e.

$$\max_{f, \Delta f} \ \Psi(f, \Delta f). \tag{2}$$

Different features such as the kurtosis of the time signal [39], the kurtosis of the cyclic spectrum [37], the L2/L1-norm [43], the spectral negentropy [44], the ratio-of-cyclic content [60], the indicator-of-second order cyclostationarity (ICS2) [36], the amount of novel information in frequency bands [27, 52, 54], the envelope harmonic-to-noise ratio [61], the Gini index [62], and the classification accuracy [51] can be used to identify informative frequency bands. The blind features (e.g. kurtosis) have the advantage that they do not require any prior knowledge before being implemented, while in contrast, the targeted methods (e.g. ICS2) require the rotational speed and the fault frequencies of the damaged components to be known a priori. The vibration signals acquired from mining machines typically contain non-Gaussian noise, which makes it necessary to carefully select the features for identifying informative frequency bands [38, 63, 64].

In this work, the Instantaneous Power Spectrum (IPS) and the Cyclic Modulation Spectrum (CMS), both linked to the Short-Time Fourier Transform (STFT), are used to construct feature planes for the different combinations of the spectral frequency f and the bandwidth Δf. This would allow us to perform frequency band identification with temporal blind, spectral blind and targeted features under time-varying operating conditions using the same framework. This is in contrast to using the order-frequency spectral coherence for constructing the feature plane (e.g. [48, 49]). Hence, brief overviews of the STFT, IPS and CMS are given in the next subsection, whereafter the different features considered in this work are discussed. The reader is referred to Ref. [12, 56, 65] for a more detailed overview of these estimators. Lastly, the framework is presented in Section 2.3.

2.1. STFT-based estimators

The Short-Time Fourier Transform (STFT) of the discrete time domain signal $\boldsymbol{x} \in \mathbb{R}^{N_x}$ is given by [66]

$$X_{TF}[m, k; \Delta f] = \sum_{b=0}^{N_w-1} x[m \cdot R + b] \cdot w[b] \cdot e^{-2\pi j b \frac{f_k}{f_s}}. \tag{3}$$

In Equation (3), the value of the STFT at a time of $t_m = m \cdot \Delta t_{TF}$, with $m = 0, 1, \ldots, M_{TF}-1$, and a frequency of $f_k = k \cdot \Delta f_{TF}$, with $k = 0, 1, \ldots, N_w-1$ is denoted $X_{TF}[m, k; \Delta f] \in \mathbb{C}$. In Equation (3), $\boldsymbol{w}$ is a symmetric window such as a Hamming window, N_w is the num-

ber of time increments, and R is the overlap between successive windows. The STFT adheres to the uncertainty principle, which means that there is a compromise between the time resolution Δt_{TF} and the frequency resolution Δf_{TF} that are attainable by the Time-Frequency STFT (TF-STFT). The subscript TF of $X_{TF}[m, k; \Delta f]$ emphasises that the distribution is on a time-frequency plane and it also indicates the order of the variables in $X_{TF}[m, k; \Delta f]$, i.e. m corresponds to the time-axis and k corresponds to the frequency axis.

The corresponding Time-Frequency Instantaneous Power Spectrum (TF-IPS) of the signal can then be estimated with [56]

$$I_{TF}[m, k; \Delta f] = \frac{1}{||w||^2 \cdot f_s} X_{TF}[m, k; \Delta f] X^*_{TF}[m, k; \Delta f], \tag{4}$$

where the factor $(||w||^2 \cdot f_s)^{-1}$ ensures that the spectrum is calibrated and the superscript * denotes the complex conjugate. The Power Spectral Density (PSD) can subsequently be estimated as the time-average of the IPS, i.e. [33]

$$P_{TF}[k; \Delta f] = \frac{1}{M_{TF}} \sum_{m=0}^{M_{TF}-1} I_{TF}[m, k; \Delta f], \tag{5}$$

or more succinctly denoted $P_{TF}[k] = \big\langle I_{TF}[m, k] \big\rangle_m$.

The impulses generated by rotating machine damage tend to excite structural resonances, which means that there will be cyclostationary components in specific bands of the instantaneous power spectrum [21, 22]. These periodicities can be detected with the Cyclic Modulation Spectrum (CMS) [56, 65, 66]

$$C_{FF}[a, k; \Delta f] = \frac{1}{M_{TF}} \sum_{m=0}^{M_{TF}-1} I_{TF}[m, k; \Delta f] \cdot e^{-2\pi j \frac{ma}{M_{TF}}}, \tag{6}$$

which is a bi-frequency distribution as indicated by the subscript FF over cyclic frequencies $\alpha_a = a \cdot \Delta\alpha$, with $a = 0, 1, \ldots M_{TF} - 1$, and spectral frequencies f_k. Even though the CMS is computationally fast to calculate, it is a biased estimator of the spectral correlation [55]. Recently, estimators of the spectral correlation were proposed which are much faster than the Welch estimator of the spectral correlation and are not biased like the CMS [66, 67]. However, their investigation is beyond the scope of this work.

Under time-varying speed conditions, vibration signals lose their time and angle cyclostationary characteristics, making TF-based estimators ill-suited [56]. An example of

this is shown in Figures 1(a) and 1(d) for a synthetic signal emulating a ramp-up scenario. The CMS spectrum in Figure 1(d) contains much smearing which makes it difficult to detect the impulses. It is possible to order track the signal under mild speed fluctuations, however, this would result in the spectral order axis to smear under large speed conditions as seen in Figures 1(b) and 1(e). This is because the signal contains angle-time cyclo-stationary properties, i.e. the impulses are periodic in the angle domain, but manifest in time-invariant frequency bands [55–57]. This would result in the damage components to lose their repetitive transient signature when considering a specific spectral frequency band. Ultimately, the signal-to-noise ratio of the components-of-interest is reduced by using the angle-order framework and this could result in the wrong frequency band to be identified. Hence, Angle-Frequency (AF) estimators [55–57] need to be used to ensure that consistent representations are obtained for analysing the signals under large time-varying speed conditions. This is highlighted in Figures 1(c) and 1(f).

The AF-IPS is obtained by order tracking the TF-IPS [56]

$$I_{AF}[u, k; \Delta f] = \mathrm{OT}_{m \to u}\{I_{TF}[m, k; \Delta f]\}, \tag{7}$$

where $m \to u$ indicates that the time index m is converted to an angle index u in the order tracking process. Order tracking can be performed by using the measured speed or phase of the signal [68] or with tacholess order tracking methods [69]. The Order-Frequency CMS (OFCMS) [56]

$$C_{OF}[a, k; \Delta f] = \frac{1}{N_u} \sum_{u=1}^{N_u - 1} I_{AF}[u, k; \Delta f] \cdot e^{-2\pi j u a / N_u}, \tag{8}$$

can then be used to detect periodicities in specific frequency bands. A detailed analysis of this estimator as well as the corresponding Matlab code is provided in Ref. [55]. Since the STFT adheres to the uncertainty principle, it is only possible to obtain reliable estimates with the OFCMS for cyclic orders $\alpha < \alpha_{cut}$, where the cut-off frequency is given by [56]

$$\alpha_{cut} = \pi \cdot \Delta f_{AF} \cdot \frac{\bar{\omega}}{||\omega||_2^2}. \tag{9}$$

The frequency resolution of the AF-IPS or OFCMS is denoted by Δf_{AF}, while $\bar{\omega}$ is the mean rotational speed and $||\omega||_2$ denotes the L2-norm of the speed. An equivalent limit α_{cut} is present for the FF-CMS, an estimate that is implicitly used in some conventional

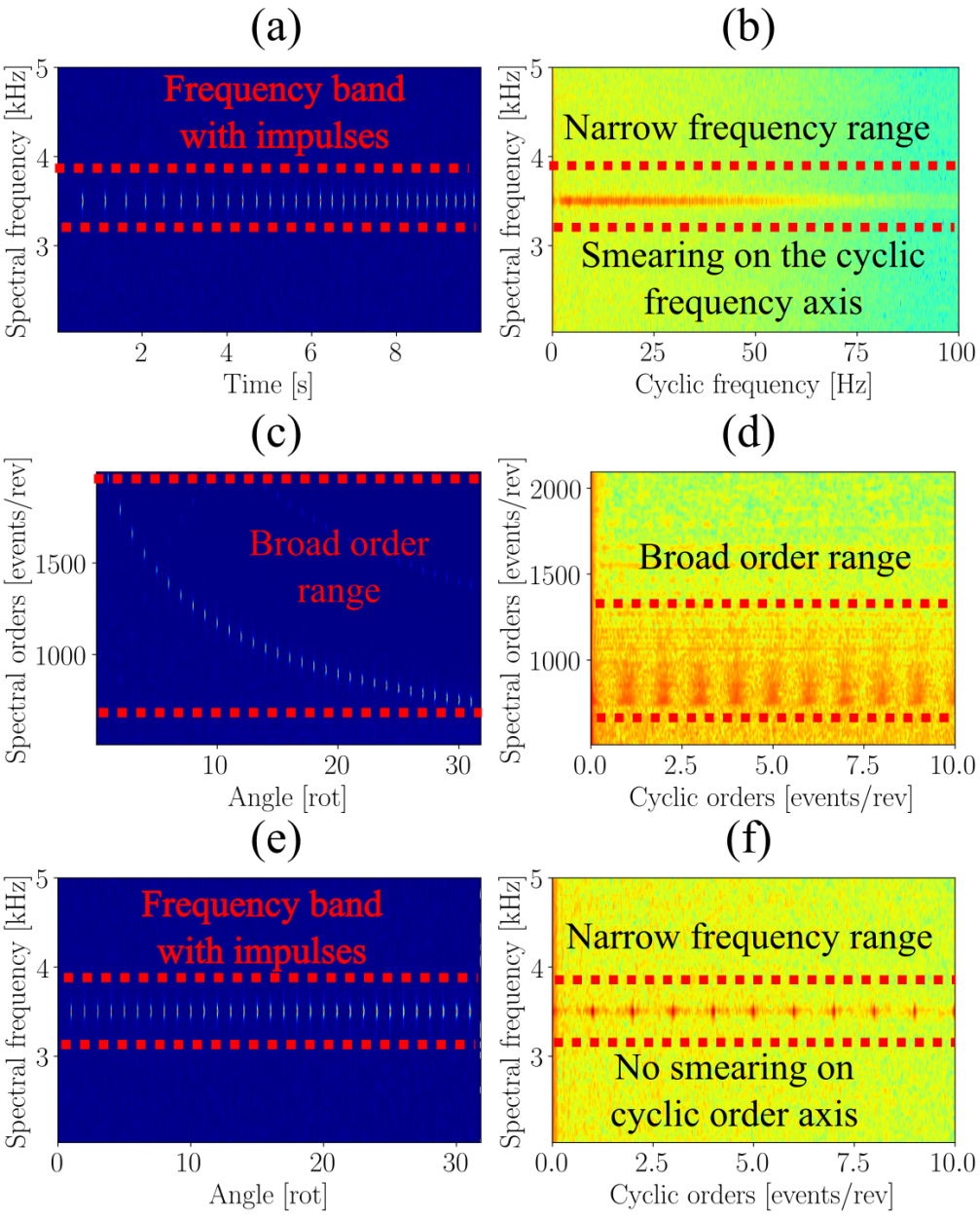

Figure 1: The instantaneous power spectrum and cyclic modulation spectrum of a synthetic signal, which simulates a train-of-impulses undergoing a ramp-up scenario, are presented for different estimators. (a) Time-Frequency Instantaneous Power Spectrum (TF-IPS); (b) Frequency-Frequency Cyclic Modulation Spectrum (FF-CMS); (c) Angle-Order Instantaneous Power Spectrum (AO-IPS); (d) Order-Order Cyclic Modulation Spectrum (OO-CMS); (e) Angle-Frequency Instantaneous Power Spectrum (AF-IPS); (f) Order-Frequency Cyclic Modulation Spectrum (OFCMS).

FBI methods. This means that the applicability of these CMS-based estimators depends on the rotational speed of the machine and care needs to be taken when the characteristic orders of the components-of-interest are large.

2.2. Features

Damaged machine components could result in the signals to become more leptokurtic, it could result in an increase in cyclostationarity and it could result in the signals' spectra to become more sparse. Therefore, there many potential scalars that can be used to identify the frequency bands with potential damage information. These features (also referred to as health indices or indicators) can be extracted from the spectral frequency bands of the IPS or the CMS to identify the informative frequency bands. The performance of the frequency band identification method is much dependent on the feature used to construct the feature plane [36, 62]. Since time-frequency, angle-order or angle-frequency estimators can be used in FBI methods, no distinctions are made between the domains of the different estimators in this section.

2.2.1. Kurtogram

The kurtogram

$$\Psi_{kurt}(f_k, \Delta f) = \frac{\left\langle |I[n,k;\Delta f]|^2 \right\rangle_n}{|P[k;\Delta f]|^2} - c, \tag{10}$$

was proposed in Refs. [33, 35, 39] as a method to automatically determine the frequency band that maximises the impulsivity in the signal. It has been successful under constant and time-varying speed conditions, however, it is very sensitive to non-repetitive transients, which could lead to frequency bands without damage information to be identified, and its value decreases with cyclic frequency [37, 44]. The constant c is used to ensure that $\Psi_{kurt}[n,k] = 0$ if the signal is Gaussian, however, for the purposes of the frequency band identification problem, the constant does not influence the optimisation problem. The kurtosis of the cyclic spectrum, as opposed to the temporal signal, has been used to overcome the inability of the conventional kurtogram to distinguish between non-periodic and periodic transients [70].

2.2.2. Infogram

The infogram uses the spectral negentropy to identify informative frequency bands. The infogram can be calculated based on the squared envelope of the signal (i.e. the instantaneous power) which is used to obtain the Squared Envelope (SE) infogram [44]

$$\Psi_{SE}(f_k, \Delta f) = \left\langle \frac{|I[n,k;\Delta f]|^2}{\left\langle |I[n,k;\Delta f]|^2 \right\rangle_n} \ln \left(\frac{|I[n,k;\Delta f]|^2}{\left\langle |I[n,k;\Delta f]|^2 \right\rangle_n} \right) \right\rangle_n, \tag{11}$$

which measures the degree-of-organisation in the time (or angle) domain of the bandlimited signal [44]. The degree-of-organisation in the cyclic spectrum can be calculated with the SES infogram [44]

$$\Psi_{SES}(f_k, \Delta f) = \left\langle \frac{|C[a,k;\Delta f]|^2}{\left\langle |C[a,k;\Delta f]|^2 \right\rangle_a} \ln \left(\frac{|C[a,k;\Delta f]|^2}{\left\langle |C[a,k;\Delta f]|^2 \right\rangle_a} \right) \right\rangle_a. \tag{12}$$

The SE infogram is often maximised by similar phenomena as the kurtogram and therefore only the SES infogram is considered in this work. Wang et al. [71] presented a unified framework for the spectral kurtosis, the spectral negentropy, the spectral Gini index and spectral smoothness index, where the aforementioned statistics can be obtained from the sum of the normalised squared envelope.

2.2.3. Sparsogram

The impulses, generated by damaged rotating machine components such as bearings, manifest in the cyclic spectrum at their cyclic frequency (or orders) and its harmonics. These signal components increase the sparsity of the cyclic spectrum and therefore the sparsogram can be used to identify frequency bands that contain much fault information. Tse and Wang [43] proposed that the L2/L1-norm should be used as a sparsity measure, which is used to construct the sparsogram. We used the following feature to construct the sparsogram

$$\Psi_{L2/L1}(f_k, \Delta f) = \sqrt{N_a} \cdot \frac{||C[a,k;\Delta f]||_2}{||C[a,k;\Delta f]||_1}, \tag{13}$$

the factor $\sqrt{N_a}$ is added to correct for the bias of the L2/L1 ratio [62] and this makes a significant difference in the frequency band identification problem. The L2- and L1-norms, denoted by $||C[a,k;\Delta f]||_2$ and $||C[a,k;\Delta f]||_1$, respectively are calculated over the a variable, with the OFCMS having N_a values in each frequency band.

2.2.4. ICS2gram

The ICS2gram is based on a cyclostationary indicator of the second-order [36]

$$\Psi_{ICS2}(f_k, \Delta f) = \sum_{a \in \mathcal{A}} \frac{|C[a, k; \Delta f]|^2}{|C[0, k; \Delta f]|^2}, \tag{14}$$

where $\mathcal{A}$ denotes the indices of the cyclic components-of-interest. The ICS2 is a powerful condition indicator for rotating machine condition monitoring [36, 72]. In the work of Ref. [73], the ICS2 was shown to be a good indicator to determine the wear mechanism and it could also detect the severity of the wear.

The estimator as presented in Equation (14) could lead to sub-optimal estimations due to the picket-fence effect and the actual cyclic orders of the components-of-interest could be slightly different from the analytical cyclic orders due to slip for example. Hence, a more appropriate estimator of the ICS2gram is given by [36]

$$\Psi_{ICS2}(f_k, \Delta f) = \sum_{h=1}^{N_h} \frac{\max\{|C[a, k; \Delta f]|^2\}_{a \in \mathcal{A}_h}}{|C[0, k; \Delta f]|^2}, \tag{15}$$

where $\mathcal{A}_h$ is the set of indices associated with the hth harmonic and given by

$$\mathcal{A}_h = \left\{ a \in \mathbb{N} | h \cdot \left(1 - \frac{\kappa}{2}\right) \cdot \alpha_c \leq \alpha_a \leq h \cdot \alpha_c \left(1 + \frac{\kappa}{2}\right) \right\}. \tag{16}$$

The analytical cyclic order of the component-of-interest is denoted α_c and the cyclic order tolerance is governed by the factor κ. The following notation is used in Equation (15)

$$\{x[n]\}_{n \in \{0,1,\ldots,N_x-1\}} = \{x[0], x[1], \ldots, x[N_x - 1]\}, \tag{17}$$

where $\max\{x[n]\}_{n \in \{0,1,\ldots,N_x-1\}}$ would return the maximum value in the set given by Equation (17). This means that in Equation (15), the hth harmonic of the signal component-of-interest is defined as the maximum component in the cyclic order band $h \cdot \left(1 - \frac{\kappa}{2}\right) \cdot \alpha_c \leq \alpha_a \leq h \cdot \alpha_c \left(1 + \frac{\kappa}{2}\right)$. If κ is too small, it would be equivalent to using Equation (14), while a too large κ would result in other signal components to be perceived as the component-of-interest and could lead to the wrong frequency band being detected. Bearing slip for example could result in 1-2% variation from the mean frequency of the component-of-interest [20] and therefore, in this work, $\kappa = 0.02$ for all considered cases.

2.2.5. Log-Cycligram

In the paper by Smith et al. [36], the authors also proposed the log-cycligram as an estimator. The log-cycligram uses the cyclic spectrum of the logarithm of the envelope instead of the envelope in the calculation of the cyclic spectrum, which makes it more robust to non-Gaussian noise [36]. The Log-CycliGram (LCG) is ultimately estimated with [36]

$$\Psi_{LCG}(f_k, \Delta f) = \sum_{h=1}^{N_h} \max\{|CL[a, k; \Delta f]|^2\}_{a \in \mathcal{A}_h}, \tag{18}$$

where $CL[a, k; \Delta f]$ denotes the CMS calculated with the logarithm of the IPS.

2.2.6. IFBI$_\alpha$gram

The IFBI$_\alpha$gram [59]

$$\Psi_{IFBI}(f_k, \Delta f) = \sum_{h=1}^{N_h} \frac{\max\{|C[a, k; \Delta f]|\}_{a \in \mathcal{A}_h}}{\text{median}\{|C[a, k; \Delta f]|\}_{a \in \mathcal{B}_h}}, \tag{19}$$

calculates the signal-to-noise ratio in the cyclic spectrum to identify frequency bands where the component-of-interest is most prominent. In the original paper [59], the OFSCoh was used to estimate the IFBI$_\alpha$gram, where the OFCMS is used as an estimator for the first time in this paper. The numerator is exactly the same as the ICS2gram in Equation (15), however, the denominator estimates the localised noise level with the median. The median of the cyclic spectrum associated with the indices

$$\mathcal{B}_h = \left\{ a \in \mathbb{N}^+ | h \cdot \alpha_c - 1 \leq \alpha_a \leq h \cdot \alpha_c + 1 \right\}, \tag{20}$$

is calculated to estimate the noise level. The median is more robust to spurious signal components and sidebands than other measures of central tendency and is therefore expected to be a more reliable estimate of the noise level in the cyclic spectrum, as it would be less affected by the presence of sparse components [49]. Since the IFBI$_\alpha$gram is estimated with the same estimator as ICS2gram and the log-cycligram, i.e., the CMS, it is possible to compare the performance of the features under time-varying operating conditions.

2.3. Application of FBI methods under time-varying operating conditions

Due to the angle-time cyclostationary properties of the impacts generated by the damaged components [55, 57], we propose that frequency band identification methods should

be applied as shown in Figure 2 under time-varying operating conditions to ensure that a consistent feature plane is obtained. The STFT and TF-IPS are calculated for a specific

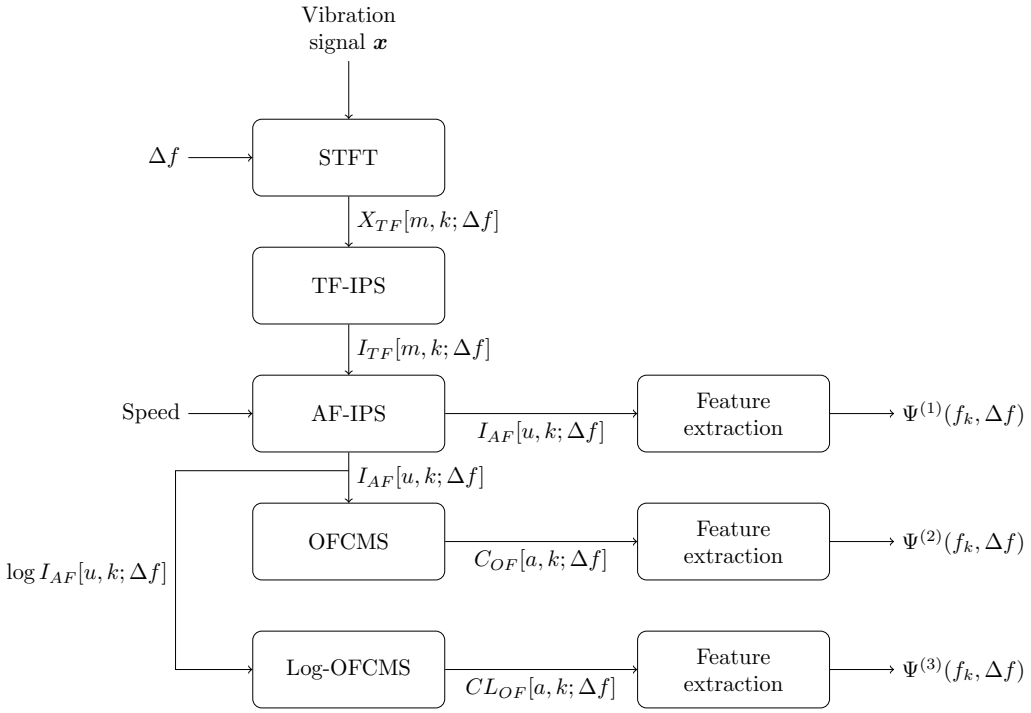

Figure 2: A broad overview of the proposed framework that can be used to extract three classes of narrowband features under time-varying operating conditions. The three identified classes are as follows: $\Psi^{(1)}(f_k,\Delta f)$ denotes the feature plane obtained from angular features (e.g. kurtogram); $\Psi^{(2)}(f_k,\Delta f)$ denotes to features obtained from spectral features (e.g. sparsogram or ICS2gram); and $\Psi^{(3)}(f_k,\Delta f)$ obtained from spectral logarithm features (e.g. log-cycligram).

frequency resolution Δf, whereafter the AF-IPS, the OFCMS or the Log-OFCMS can be calculated depending on the class of the feature under consideration. This process can be repeated for all the frequency resolutions Δf under consideration to construct a feature plane $\Psi(f_k,\Delta f)$. The features considered in the previous section can be classified as follows using the classes in Figure 2:

- Angular features, denoted $\Psi^{(1)}(f_k,\Delta f)$, include the conventional kurtogram and SE infogram.
- Spectral features, denoted $\Psi^{(2)}(f_k,\Delta f)$, include the sparsogram, the SES infogram, the ICS2gram and the IFBI$_\alpha$gram.
- Spectral logarithm features, denoted $\Psi^{(3)}(f_k,\Delta f)$, include the log-cycligram.

Ultimately, the specific feature is extracted from each frequency band to construct the feature plane $\Psi(f_k, \Delta f)$, which is subsequently maximised to identify the informative frequency band using Equation (2). In this work, blind methods refer to frequency band identification methods that do not require the cyclic orders of the components-of-interest to be known a priori. In contrast, targeted methods refer to frequency band identification methods that target the cyclic orders of the components-of-interest to find the informative frequency bands [36].

The framework proposed in Figure 2, which relies on the theory developed by Abboud et al. [55, 57], is a subtle extension of conventional frequency band identification methods, but is essential to ensure that the angle-time cyclostationary properties of the signals are preserved under time-varying operating conditions. This allows the performance of the angular, spectral, and spectral logarithm features to be compared using the same framework under time-varying operating conditions.

In the next section, the IFBI$_\alpha$gram is compared against different features using the proposed framework on numerical gearbox data acquired under time-varying operating conditions. Thereafter, in Section 4, the IFBI$_\alpha$gram is compared to other methods using the proposed framework on two experimental gearbox datasets, both acquired under time-varying operating conditions.

3. Numerical gearbox data

The phenomenological gearbox model used by Abboud et al. [23] and extended by Schmidt et al. [27] to include inner race bearing damage, is used in this work to compare the performance of the different methods. In the next section, a brief overview of the model is given. Thereafter, the feature planes and the resulting squared envelope spectra of the different frequency band identification methods are compared on a single signal in Section 3.2. Lastly, in Section 3.3, the performance of the different methods are compared by incrementally increasing the bearing damage component under time-varying operating conditions.

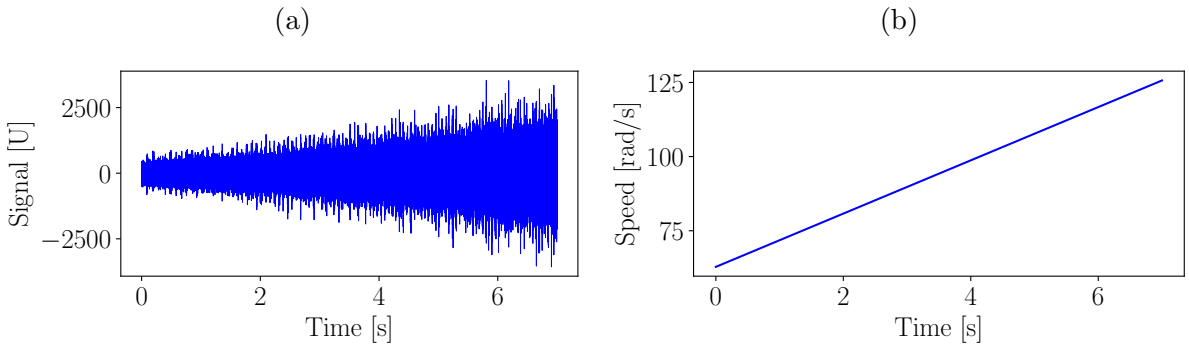

Figure 3: The casing vibration signal and the rotational speed that were used to generate the data are presented in Figures 3(a) and 3(b) respectively. Since the signal of the phenomenological gearbox model is not calibrated to have specific units, the units of the signal and its instantaneous power are U and U^2 respectively.

3.1. Overview of model

The measured signal of the phenomenological bearing model is decomposed in terms of five independent components [27]

$$x_c = x_{gmc}(t) + x_{bo}(t) + x_{bi}(t) + x_{dgd}(t) + x_n(t), \tag{21}$$

where $x_{gmc}(t)$ is the deterministic gear component attributed to gear meshing, $x_{bo}(t)$ is the outer racing bearing damage component, $x_{bi}(t)$ is the inner race bearing damage component, $x_{dgd}(t)$ is the distributed gear damage component and $x_n(t)$ is the broad band noise component. The cyclic order of the gear is 1.0 shaft order, the Ball-Pass Order of the Outer race (BPOO) component of the bearing is 4.12 shaft orders, and the Ball-Pass Order of the Inner race (BPOI) component of the damaged bearing is 5.88 shaft orders. More information related to the model, such as the signal-to-noise ratios of the different components, can be found in Appendix A. The gear components are purposefully made very dominant to mask the weak bearing damage components and therefore the objective is to detect the weak bearing components despite the dominant gear component.

The casing vibration signal and the rotational speed of the shaft are presented in Figure 3. The time-varying speed in Figure 3 necessitates using the proposed framework.

3.2. Frequency Band Identification: Illustration on a single signal

The following FBI methods are applied on the signal in Figure 3: IFBI$_\alpha$gram, ICS2gram, Log-Cycligram, SES infogram, kurtogram and sparsogram. For the targeted methods, the cyclic order vector is $\boldsymbol{\alpha} = [1.0, 2.0, 3.0]$ for the distributed gear damage component, $\boldsymbol{\alpha} = [4.12, 8.24, 12.36]$ for the outer race bearing damage component, and $\boldsymbol{\alpha} = [5.88, 11.76, 17.64]$ for the inner race bearing components. The blind methods do not require this information when identifying the frequency bands, however, the signal component that is extracted by the blind method needs to be determined a posteriori (i.e. by looking for evidence of cyclostationary components in the filtered signal).

The resulting feature planes and the Squared Envelope Spectra (SES), obtained by bandpass filtering the signal with the parameters identified by maximising the features, are presented for the IFBI$_\alpha$gram in Figure 4. The vertical markers in the SES indicate the position of the cyclic components that were targeted as well as all related harmonics. The first harmonic of the distributed gear damage component is very clearly seen in Figure 4(d). The feature plane of the distributed gear damage component, shown in Figure 4(a), contains two frequency bands; the lower frequency band is attributed to the gear component, while the higher frequency band is associated with the inner race bearing damage component. The inner race bearing damage component is seen because it contains modulation from the damage moving through the load zone as the shaft is rotating. The sidebands are spaced at the rotational order of the shaft and the squared envelope spectrum also contains a fundamental component related to the rotation of the shaft [27]. The ballpass inner race components as well as their sidebands are very prominent in Figure 4(f). The outer race bearing component and its four harmonics are also very prominent in the cyclic spectrum in Figure 4(e). Hence, the IFBI$_\alpha$gram is able to identify the frequency bands of the targeted components very well.

The same analysis was performed for the ICS2gram with the results presented in Figure 5. The ICS2gram of the distributed gear damage component also detects the inner race bearing damage component in Figure 5(a), but the inner race bearing damage component is much weaker when compared to the IFBI$_\alpha$gram. This highlights two things; the IFBI$_\alpha$gram is more sensitive to the presence of cyclostationary components and the targeted methods could be affected by periodic components attributed to other machine

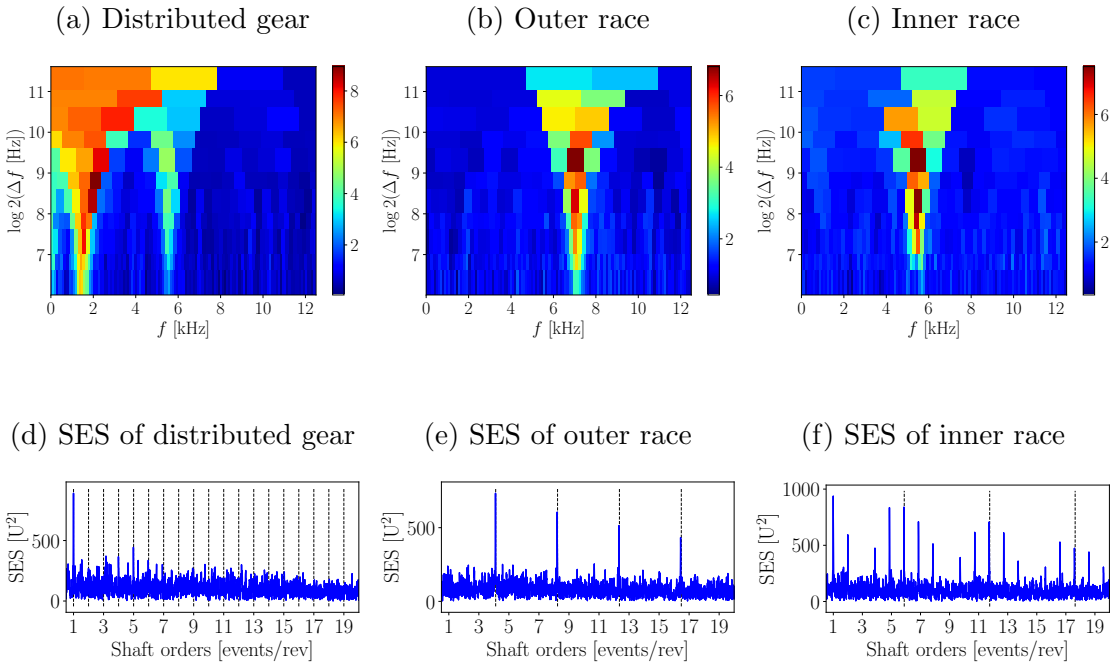

Figure 4: The IFBI$_\alpha$gram and the corresponding SES of the filtered signal for different targeted cyclic orders applied to the phenomenological gearbox model's signal. (a) IFBI$_\alpha$gram for the distributed gear damage component with $\alpha_c = 1.0$; (b) IFBI$_\alpha$gram for the outer race bearing damage component with $\alpha_c = 4.12$; (c) IFBI$_\alpha$gram for the inner race bearing damage component with $\alpha_c = 5.88$; (d) SES for the distributed gear damage component with $\alpha_c = 1.0$; (e) SES for the outer race bearing damage component with $\alpha_c = 4.12$; (f) SES for the inner race bearing damage component with $\alpha_c = 5.88$.

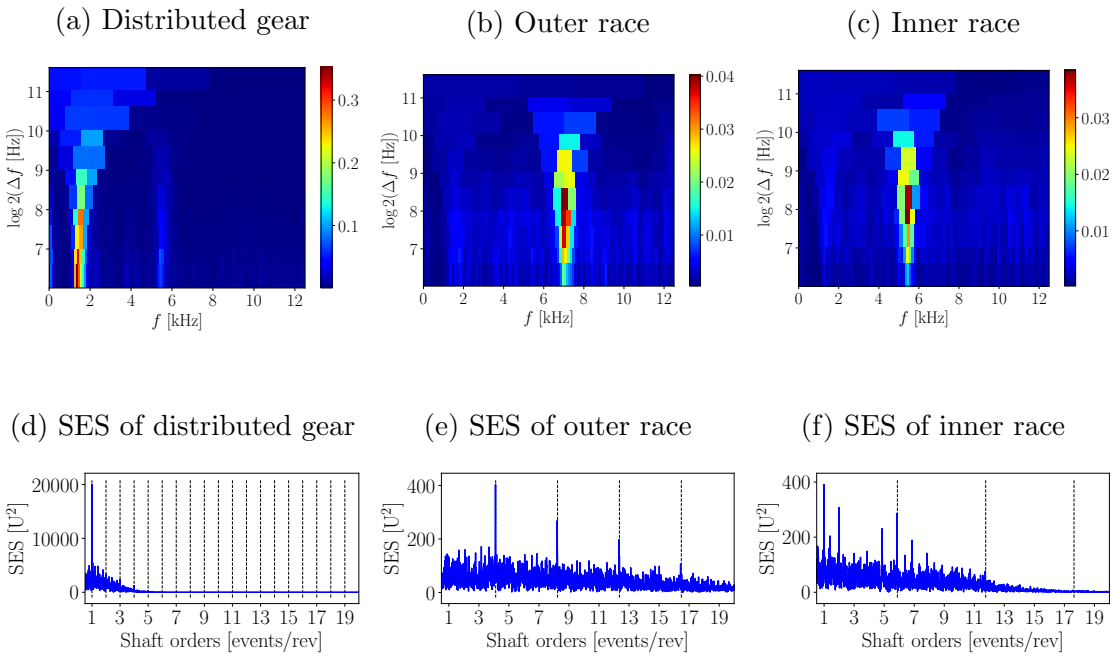

Figure 5: The ICS2gram and the corresponding SES of the filtered signal for different targeted cyclic orders applied to the phenomenological gearbox model's signal.

components if the components or their sidebands have nearly the same cyclic order as the component-of-interest. Even though the components-of-interest can be identified in the SES of the filtered signals obtained with the ICS2gram in Figure 5, only one harmonic can be seen for the inner race bearing damage case in Figure 5(f) . This is in contrast to the IFBI$_\alpha$gram, were the inner race bearing damage components were very prominent in the SES.

The log-cycligram, presented in Figure 6, performs similarly to the ICS2gram for the distributed gear damage and inner bearing damage components. In contrast, the outer race bearing damage component is more prominent in the ICS2gram, with only two harmonics present in Figure 6(e) compared to the four harmonics seen in Figure 5(e).

Lastly, the kurtogram, the sparsogram and the SES infogram are compared for the same signal on Figure 7. The squared envelope spectra do not have any marks to highlight the position of the cyclic components, because these methods are blind and the component needs to be identified by interrogating the SES. The SES obtained from all three methods contain the distributed gear component, which indicates that it is most impulsive or sparse

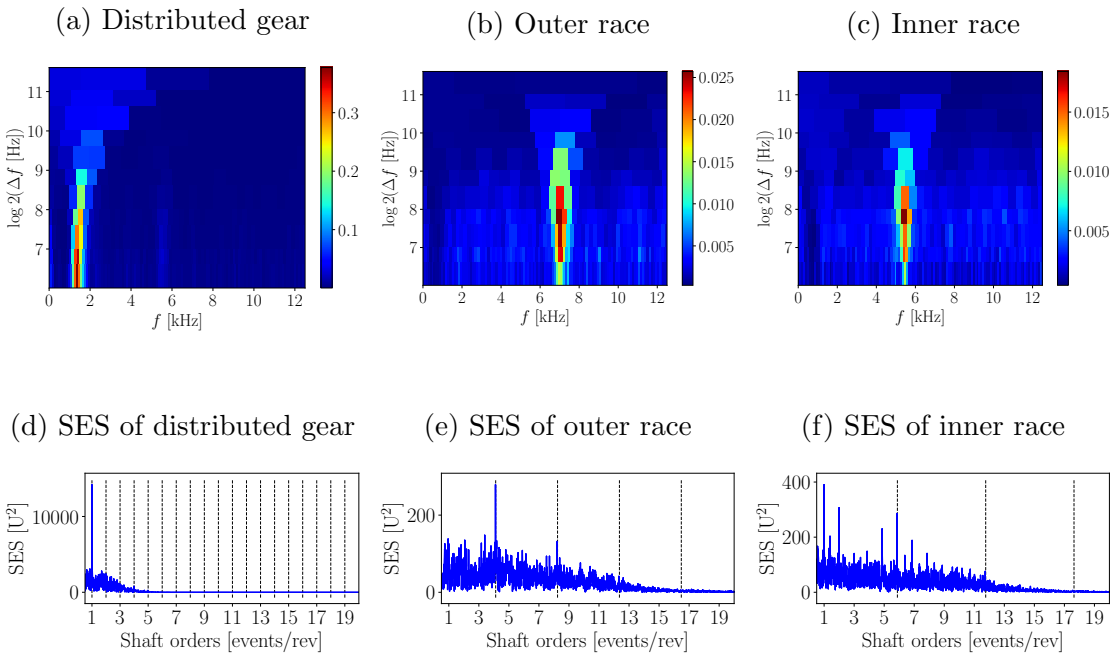

Figure 6: The log-cycligram and the corresponding SES of the filtered signal for different targeted cyclic orders applied to the phenomenological gearbox model's signal.

component in the signal.

Hence, the results indicate that the targeted methods are more sensitive to incipient damage than the blind methods, with the IFBI$_\alpha$gram performing the best at extracting the components-of-interest under time-varying operating conditions. In the next section, the magnitude of the bearing components is changed to investigate the sensitivity of the considered frequency band identification methods under time-varying operating conditions.

3.3. Frequency Band Identification: Sensitivity analysis with respect to damage

In this section, the performance of the different methods is compared by incrementally increasing the outer race bearing damage over measurement number, while the statistical properties of the distributed gear damage, gear mesh components and noise are kept constant. The signal-to-noise ratio of the bearing component is shown in Figure 8(a) over measurement number, with the corresponding speed profiles shown in Figure 8(b) for the 400 measurements considered. The SNR range enables us to critically compare the performance of the methods from a healthy bearing to a bearing with dominant impulses. The speed profile allows us to compare the performance of the methods under varying

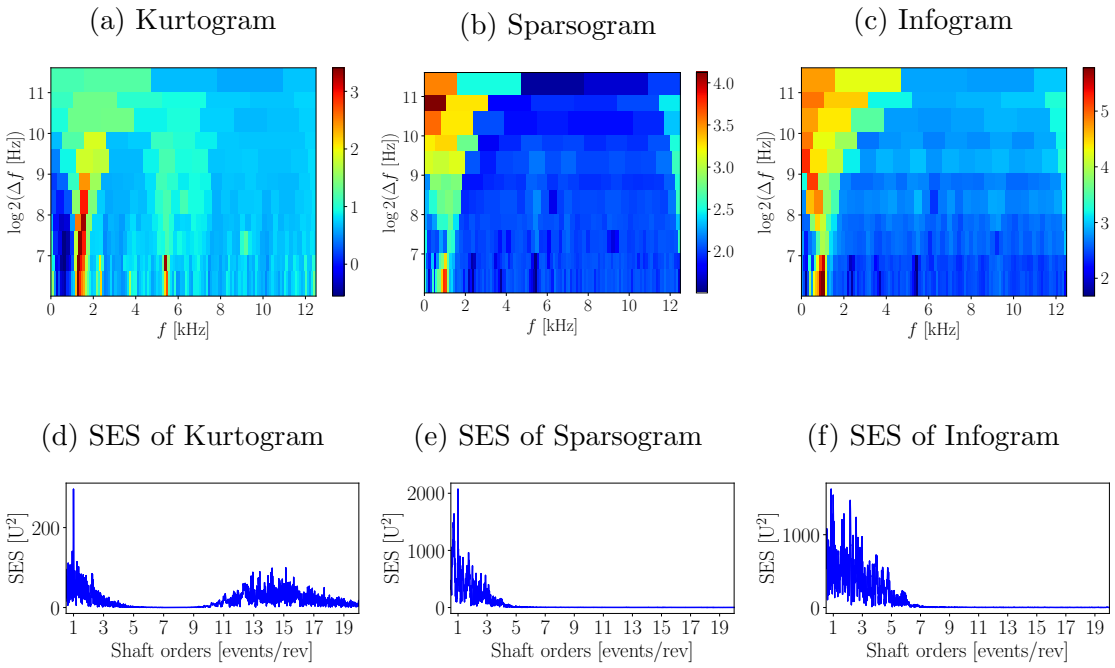

Figure 7: The result of three blind methods, the kurtogram, sparsogram and infogram are presented for the phenomenological gearbox model's signal.

operating conditions.

The RMS and the kurtosis of the raw measurements are presented in Figure 8, with only clear changes in the metrics observed after Measurement 300. The sensitivity of the RMS to speed variation is prevalent in Figure 8(c); with large variations seen in consecutive measurements. In contrast, the kurtosis is much more robust to the speed variation and a clear degradation of the bearing is seen in Figure 8(d). Even though this monotonic degradation is seldom seen in actual bearings [74, 75], it can be used to compare the performance of the different features using the proposed framework.

The centre frequency f_c of the frequency bands identified by the different FBI methods are presented in Figure 9 with the analytical centre frequencies of the outer race bearing damage and distributed gear damage components presented as well. The results indicate that for the cases where the damage component is very small, the blind features (e.g. kurtogram, SES infogram, sparsogram) and the ICS2gram identify in some cases a frequency band in the region of the distributed gear damage component. The log-cycligram and the IFBI$_\alpha$gram identifies random frequency bands for the initial measurements. The

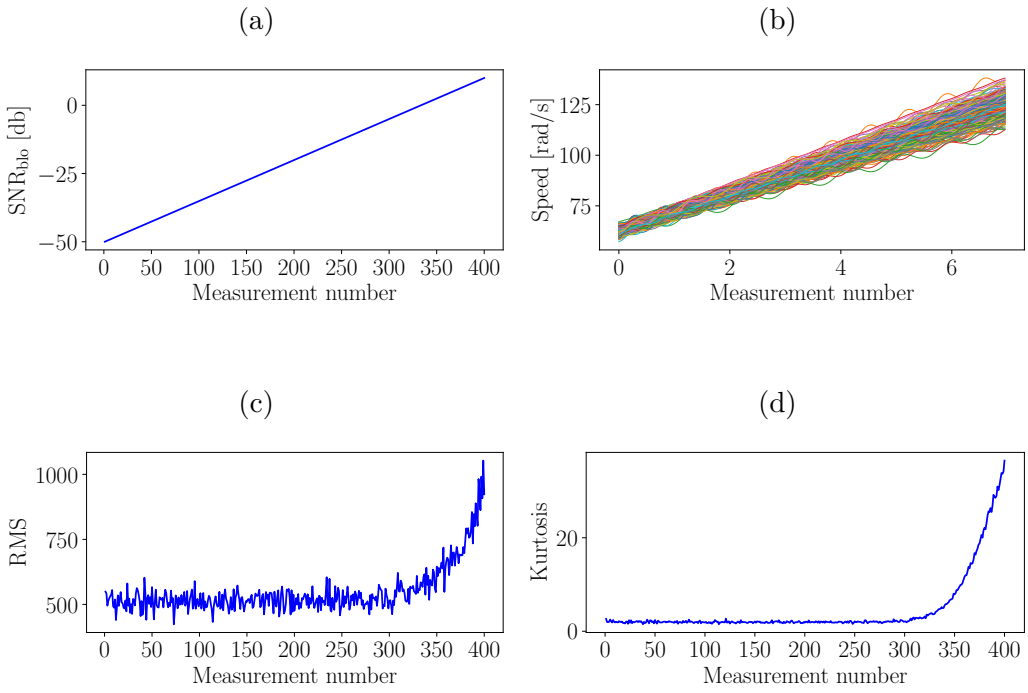

Figure 8: An overview of the dataset used in the investigation is given. (a) The Signal-to-Noise Ratio (SNR) of the Bearing Outer (BO) component is presented over measurement number. The SNR is defined as $10 \cdot \log_{10}\left(\sigma_b^2/\sigma_n^2\right)$ where σ_b^2 is the variance of the bearing component and σ_n^2 is the variance of the noise. (b) The rotational speed of the shaft is presented for the different datasets. (c) The Root-Mean-Square (RMS) of the raw vibration signals. (d) The kurtosis of the raw vibration signal.

log-cycligram only uses the peaks of the components-of-interest in the spectrum of the logarithm of the instantaneous power, while the IFBI$_\alpha$gram only uses the peaks of the component-of-interest and an estimate of the noise floor. Since the component-of-interest is non-existent in the initial measurements, the identified peaks in the cyclic spectrum are essentially random, which ultimately results in this random behaviour to be observed.

The results in Figure 9 are used to determine at which measurement the appropriate frequency band is identified. The kurtogram detects the random component at approximately the 266th measurement, the sparsogram detects it at approximately the 305th measurement, the SES infogram detects the damage at the 308th measurement, the ICS2gram detects the damage at the 185th measurement, the log-cyligram detects the damage at the 175th measurement and lastly the IFBI$_\alpha$gram detects the damage at the 179th measurement. The targeted methods detect the damage much earlier than the blind methods.

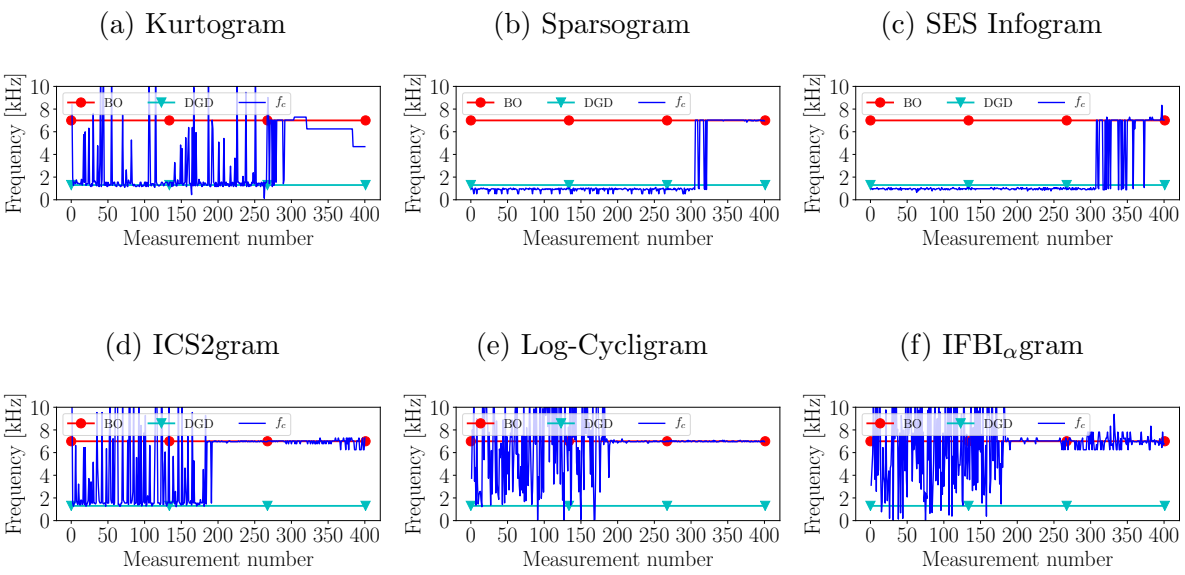

Figure 9: The centre frequency of the identified frequency band is presented over measurement number for the different frequency band identification methods. The analytical centre frequency of the Distributed Gear Damage component (DGD) and the Bearing Outer (BO) race component are presented as well.

The ICS2gram in Figure 9(d) and IFBI$_\alpha$gram in Figure 9(f) have some variation in the centre frequency for the last few measurements, while in contrast the log-cycligram in Figure 9(e) is very stable.

The maximum value of the feature plane (i.e. the feature that corresponds to the optimal frequency band) is used as a condition indicator in this work. The condition indicator is presented in Figure 10 over measurement number for the different FBI methods. The kurtogram performs the best of the blind methods, since it shows changes earlier than the sparsogram and the SES infogram. The targeted methods perform much better than the blind methods, with the damaged detected before the 200th measurement.

A threshold, calculated using the first 100 measurements and denoted by $\mu + 3 \cdot \sigma$, is compared against the smoothed condition indicator to determine the detection point of the targeted methods. The condition indicator of the ICS2gram exceeds the threshold at the 191th measurement, and both the condition indicator of the log-cycligram and the IFBI$_\alpha$gram exceed the threshold at the 181th measurement. The condition indicator of the IFBI$_\alpha$gram in Figure 11(c) seems to increase linearly from the 181th measurement, while the condition indicator of the log-cycligram in Figure 11(b) increases step-wise from

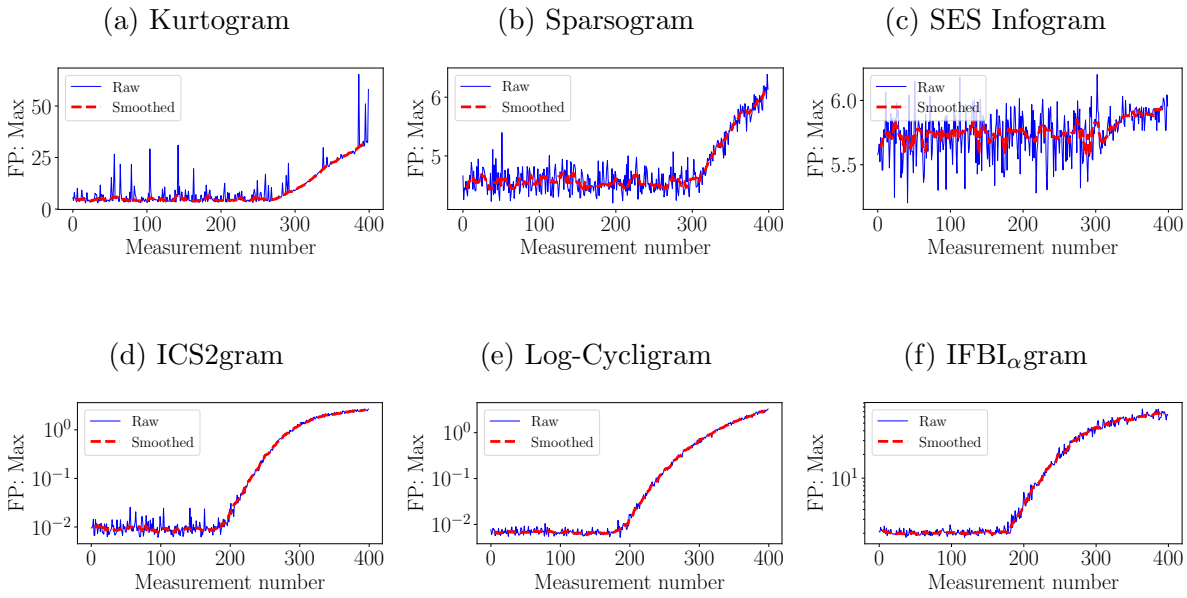

Figure 10: The maximum value of the Feature Plane (FP) is presented for the different FBI methods over measurement number. The smoothed condition indicator is obtained by applying a moving median filter with a window length of 10. The condition indicators associated with the targeted FBI methods are presented on a logarithmic scale for easier visualisation.

the 181th measurement.

In conclusion, the targeted methods perform much better than the blind methods for detecting the damage components under time-varying operating conditions; the targeted methods detect the damage at least 60 measurements earlier and the condition indicators show a clear degradation trend. Of the targeted methods, the log-cyligram and the IFBI$_\alpha$gram perform the best at detecting the damage.

In the next section, two experimental datasets are investigated to compare the performance of the methods for localised and distributed gear damage detection under time-varying operating conditions.

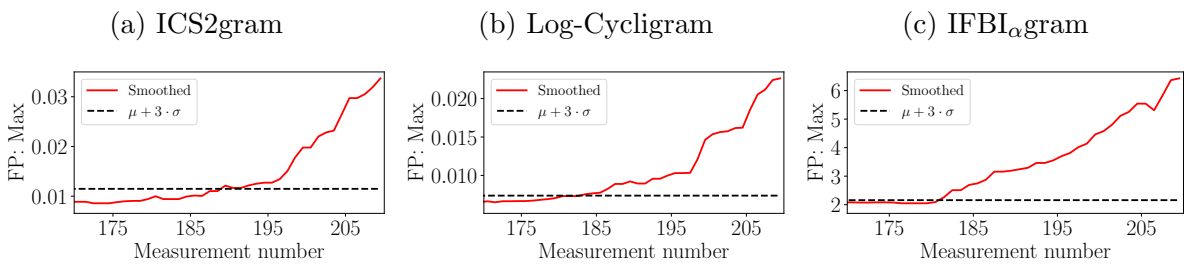

Figure 11: The smoothed estimate in Figure 10 is compared against a threshold for the three targeted features to compare the performance of the features. The parameters of the threshold $\mu+3\cdot\sigma$ are obtained from the mean μ and the standard deviation σ of the first 100 measurements.

4. Experimental gearbox data

In this section, the different FBI methods are applied on two experimental datasets with the results critically compared. In the next section, an overview of the experimental test-rig is given, whereafter a gearbox with localised gear damage is investigated in Section 4.2 and a gearbox with distributed gear damage is investigated in Section 4.3. Lastly, the OFCMS estimator of the IFBI$_\alpha$gram is compared against the OFSCoh estimator of the IFBI$_\alpha$gram in Section 4.4.

4.1. Experimental test-rig

The experimental test-rig shown in Figure 12 comprises of three helical gearboxes, an alternator and an electrical motor. The centre gearbox, indicated as the monitored gearbox, is monitored for damage with accelerometers and an optical probe and zebra tape shaft encoder are located on the coupling of the input shaft of this gearbox (i.e. S2 in Figure 12) to measure its instantaneous rotational speed. The rotational speed of the electrical motor and the load applied by the alternator are separately controlled by a personal computer. The accelerometer signal, located on the back of the monitored gearbox, is sampled at 25.6 kHz and the optical probe signal is sampled at 51.2 kHz with an OROS OR35 data acquisition system. Since a helical gearbox is being monitored, the axial component of the tri-axial component is used in this work. The time-varying operating conditions that are investigated in this section are shown in Figure 12.

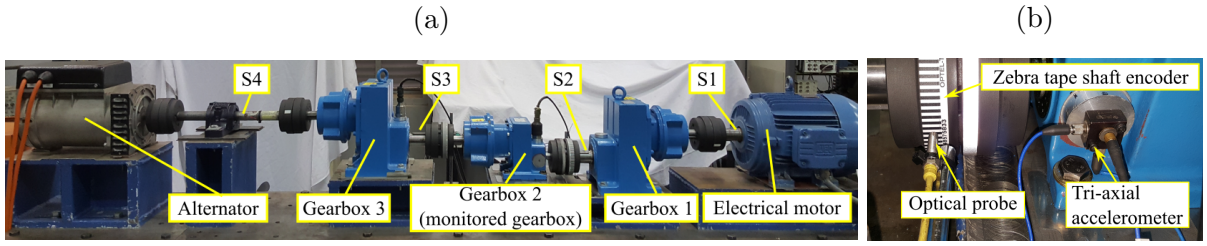

Figure 12: The experimental test-rig is shown with the important components and sensors being clearly annotated. (a) An overview of the test-rig is presented with the shaft numbers given by $S1$, $S2$, $S3$, and $S4$; (b) The back of the monitored gearbox is presented with the tri-axial accelerometer and the speed measurement equipment being highlighted.

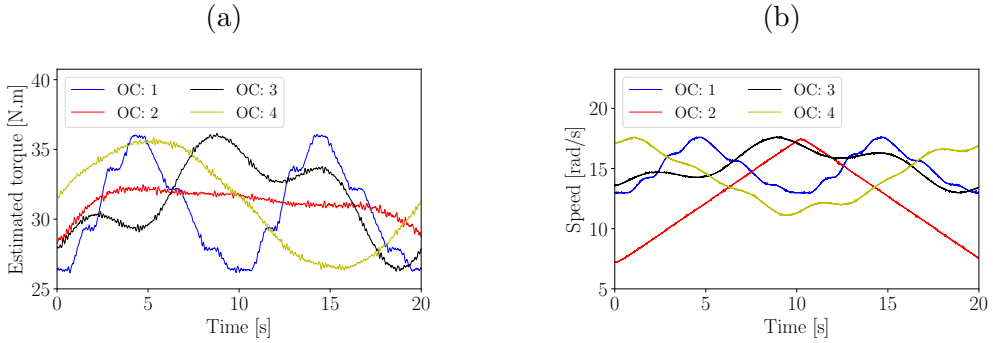

Figure 13: The operating conditions that were present at the input shaft (i.e. Shaft S2) of the monitored gearbox. In Figures 13(a) and 13(b) the estimated torque and rotational speed are presented for different Operating Condition (OC) cases respectively.

Figure 14: The gear with localised gear damage (a) before the experiment started and (b) after the fatigue experiment was completed.

4.2. Localised gear damage

Localised gear damage such as root cracks results in stress concentrations which could adversely influence the remaining useful life of the gear. Additionally, since the stiffness of the gear tooth would decrease, the adjacent gear teeth would be exposed to higher forces, which could result in further damage in the gearbox [76]. Therefore, detecting localised gear damage is extremely important to ensure that the gearbox operates as intended. Hence, an experiment was performed with a gearbox that had a gear with localised damage and a healthy pinion. The gear, seeded with damage shown in Figure 14(a), was operated for approximately twenty days before the gear tooth failed as shown in Figure 14(b). Regular measurements were taken of the gearbox while it was operating under Condition 1 shown in Figure 13. Even though the initial gear fault may seem severe (i.e. it does not constitute a root crack), it is not easy to detect the damage due to the fact that helical gears are used and the data were contaminated with impulsive components attributed to a floating bearing.

Two signals are considered in this section, with the signals and their squared envelope spectra being shown in Figure 15. Measurements 1 and 2 were respectively taken approximately 16 and 2 days before the estimated failure of the gear tooth. Since the damage is located on the gear and the gear rotates at 1.0 shaft order, it is expected that the SES would contain signal components at 1.0 shaft order and its harmonics. However, it is not possible to detect these components in the SES, which therefore erroneously indicates

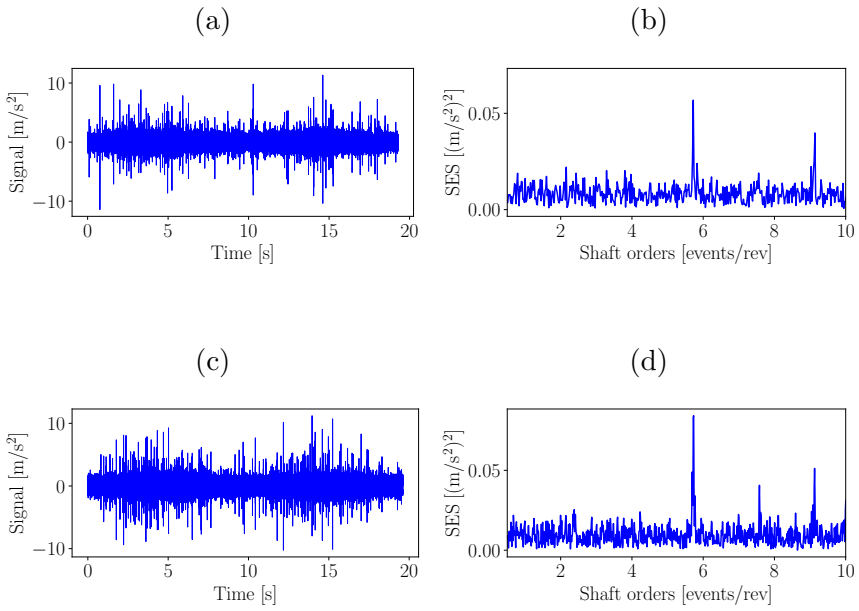

Figure 15: Two measurements are presented for the gearbox that had Localised Gear Damage (LGD). (a) Vibration signal of measurement 1; (b) SES of measurement 1; (c) Vibration signal of measurement 2; (d) SES of measurement 2.

that the gearbox is healthy. There is a strong component at 5.72 shaft orders, but this component is not associated with the damaged gearbox, since it is even present in the SES of a healthy gearbox. Therefore, FBI methods are investigated to enhance the vibration signals which could aid in detecting the damage.

The performance of the different FBI methods are compared for Measurement 1 in Figure 16. The cyclic orders of the gear $\boldsymbol{\alpha} = [1.0, 2.0, 3.0]$ are targeted by the IFBI$_\alpha$gram, ICS2gram and the log-cyclicgram. The cyclic orders of the damaged component of 1.0 and its harmonics are clearly seen in the SES of the IFBI$_\alpha$gram, however, none of the other methods are able to extract the component-of-interest sufficiently well. The ICS2gram and the kurtogram are maximised in the low energy region in the higher frequency bands, which leads to only the 5.72 component to be present in the SES. This behaviour could result from the fact that the term in the dominator of the ICS2gram and the kurtogram is the energy of the narrowband signal. The log-cycligram identifies a dominant frequency band at approximately 4 kHz, however, this band does not contain much information of the component-of-interest. The targeted methods (i.e. IFBI$_\alpha$gram, ICS2gram, log-

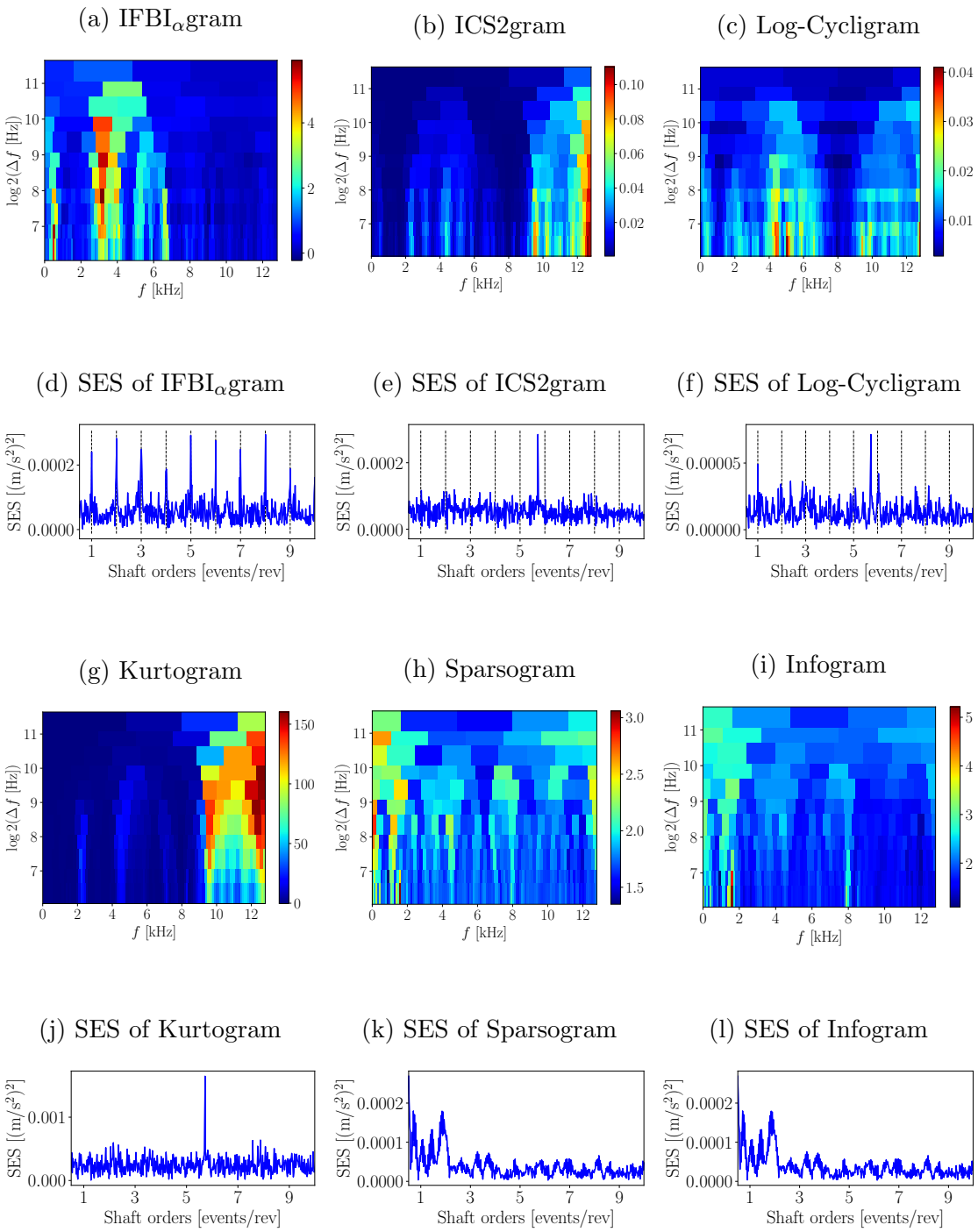

Figure 16: The feature planes and resulting SES of the filtered signals are presented for measurement 1 of the localised gear damage experiment. The feature planes are presented in (a), (b), (c), (g), (h), and (i). The SES of the bandlimited signals, with the frequency band of the filter determined by maximising the corresponding feature plane, are presented in (d), (e), (f), (j), (k), and (l).

cycligram) estimate the component-of-interest with a maximum operator. This means that any noise in the signal or the estimated cyclic spectrum, could result in the amplitude of the component-of-interest to increase, which can easily lead to the wrong frequency band to be identified. This is why the signal-to-noise measure used in the construction of the IFBI$_\alpha$gram is important when a targeted approach is used for the FBI problem. Even if a large signal component is detected in the numerator of Equation (19), it would lead to a small feature if the estimated noise level in the denominator of Equation (19) is large.

The same analysis is performed for the second measurement that is considered in this section. The gearbox was in a worse condition for this measurement, since it was taken two days before the failure of the gear tooth. Therefore, it is expected that the damage would be easier to detect. The feature planes of the different FBI methods and the associated SES are presented in Figure 17. In this second measurement, both the IFBI$_\alpha$gram and the ICS2gram are capable of identifying the best frequency band to identify the damage component, while the other methods fail to enhance the damage. The frequency band that was identified previously by the log-cycligram is detected again. The noise level of this frequency band is quite high, and since the log-cycligram only uses the maximum operator in its estimation as seen in Equation (18), it is susceptible to these frequency bands.

When comparing the feature planes obtained by the ICS2gram between the two measurements, i.e. Figures 16(e) and 17(e), it is observed that the dominant frequency band, which was erroneously identified in the first measurement, is still very dominant in the feature plane of the second measurement. This indicates that the damage would need to be further developed in this gearbox, before the correct frequency band is identified with the ICS2gram. Since the IFBI$_\alpha$gram searches for the frequency band where the damage component is the most prominent, it performed very well in detecting the localised gear damage for both measurements.

In the next section, the same analysis is applied to measurements that were taken from a gearbox with distributed gear damage.

4.3. Distributed gear damage

A healthy gear of the monitored gearbox was left in a corrosive environment for an extended period of time, which resulted in damage to develop on the surface of the gear

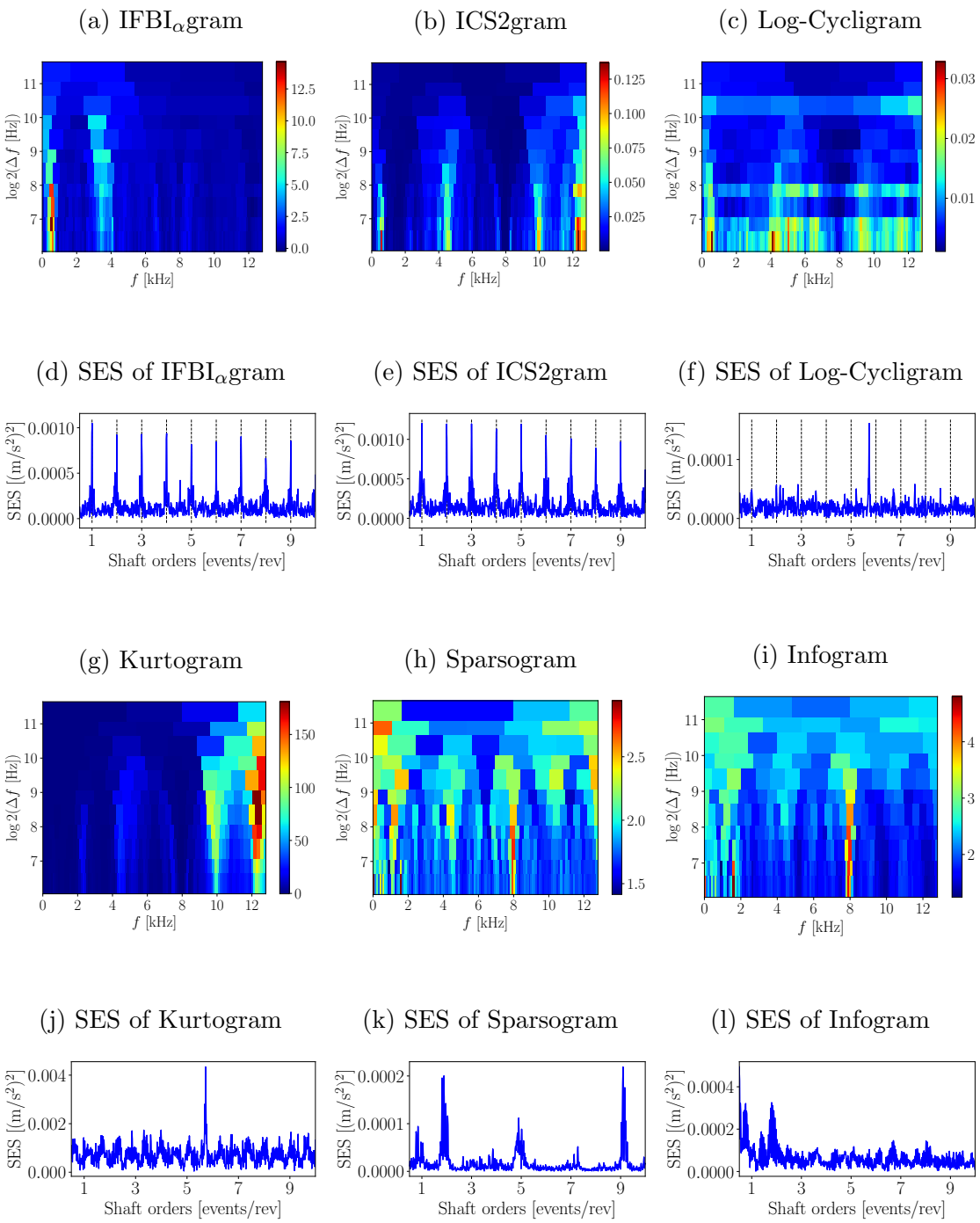

Figure 17: The feature planes and resulting SES of the filtered signals are presented for measurement 2 of the localised gear damage experiment. The feature planes are presented in (a), (b), (c), (g), (h), and (i). The SES of the bandlimited signals, with the frequency band of the filter determined by maximising the corresponding feature plane, are presented in (d), (e), (f), (j), (k), and (l).

(a)

(b)

Figure 18: The gear with distributed gear damage is presented in (a) before the experiment started and in (b) after the experiment was completed, with the failed gear teeth clearly highlighted.

as shown in Figure 18(b). Even though the damage depicted in this figure is worse than what would be expected in the early stages of gear pitting or wear (e.g. Ref. [73]), it still provides an opportunity to critically compare the performance of different FBI methods in detecting distributed gear damage under time-varying operating conditions.

The gearbox was operated with the damaged gear and an healthy pinion for a few days before localised gear damage started to develop in one of the gear teeth which resulted in its failure. After this first event, the adjacent gear teeth were exposed to larger stresses and impacts, which ultimately resulted in the adjacent gear teeth to become severely damaged as shown in Figure 18(b). Two measurements that were acquired before the failure of any gear tooth (i.e. before the first event) are analysed to determine whether the distributed gear damage can be detected. Measurement 1 was taken approximately a day before the first event, while measurement 2 was taken approximately 30 minutes before this event. In Figures 19(b) and 19(d), the SES of the Cepstrum Pre-Whitened (CPW) signals, calculated as described in Ref. [24], are investigated so that the first order cyclostationary components are attenuated which could impede the detection of the damaged gear. In

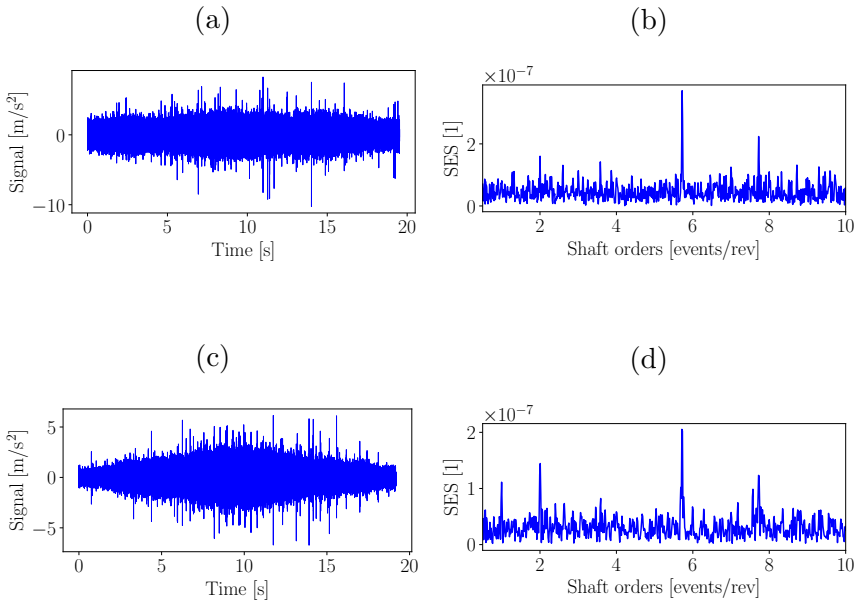

Figure 19: The raw vibration signal and SES for two measurements taken during the Distributed Gear Damage (DGD) experiment. (a) Vibration signal of measurement 1; (b) The SES of the CPW signal of measurement 1; (c) Vibration signal of measurement 2; (d) The SES of the CPW signal of measurement 2.

the SES of measurement 1, there are no clear components associated with 1.0 shaft orders and their harmonics. The SES of measurement 2 contains two harmonics associated with the gear damage (i.e. at 1.0 and 2.0 shaft orders). The suitability of the different FBI methods to enhance the gear damage is investigated in Figure 20 for the first measurement and in Figure 21 for the second measurement.

The feature planes and the SES of the different FBI methods are compared in Figure 20 for the first measurement. The targeted methods, targeted the cyclic orders associated with the gear, i.e. $\boldsymbol{\alpha} = [1.0, 2.0, 3.0]$. The IFBI$_\alpha$gram, the log-cycligram, the sparsogram and the SES infogram are capable of enhancing the signal components, while the kurtogram and the ICS2gram could not. The SES obtained with the IFBI$_\alpha$gram and the log-cycligram are much clearer than the SES obtained with the blind methods as well as the SES shown in Figure 19(b). The ICS2gram and the kurtogram are again adversely influenced by the low energy components in the high frequency regions of the signal.

The feature planes and the SES of the different FBI methods are compared in Figure 21 for the second measurement. A similar performance is obtained by the different methods as the previous measurement. A few harmonics of the gear damage are very prominent in the SES of the IFBI$_\alpha$gram and SES infogram, which is in contrast to the SES shown in Figure 19(d). Even though the log-cycligram and the sparsogram are able to detect the damaged components, the SES of the log-cycligram only contains one harmonic of the component-of-interest, while the SES of the sparsogram contains much noise which could make it difficult to detect and to diagnose the damage. The results indicate that the IFBI$_\alpha$gram and the log-cycligram are very capable of detecting the distributed gear damage, while the ICS2gram does not perform very well.

The targeted methods performed much better than the blind methods on the experimental measurements under time-varying operating conditions. This was because the signals associated with the gear damage was not the most impulsive or most sparse in the frequency bands of the signal and therefore the blind methods were easily distracted by the wrong phenomena. The IFBI$_\alpha$gram is the only targeted method that performed consistently well on all measurements. The ICS2gram was only capable of detecting the localised gear damage of the second measurement, but could not detect the localised gear damage in the first measurement and did not perform well on the distributed gear dam-

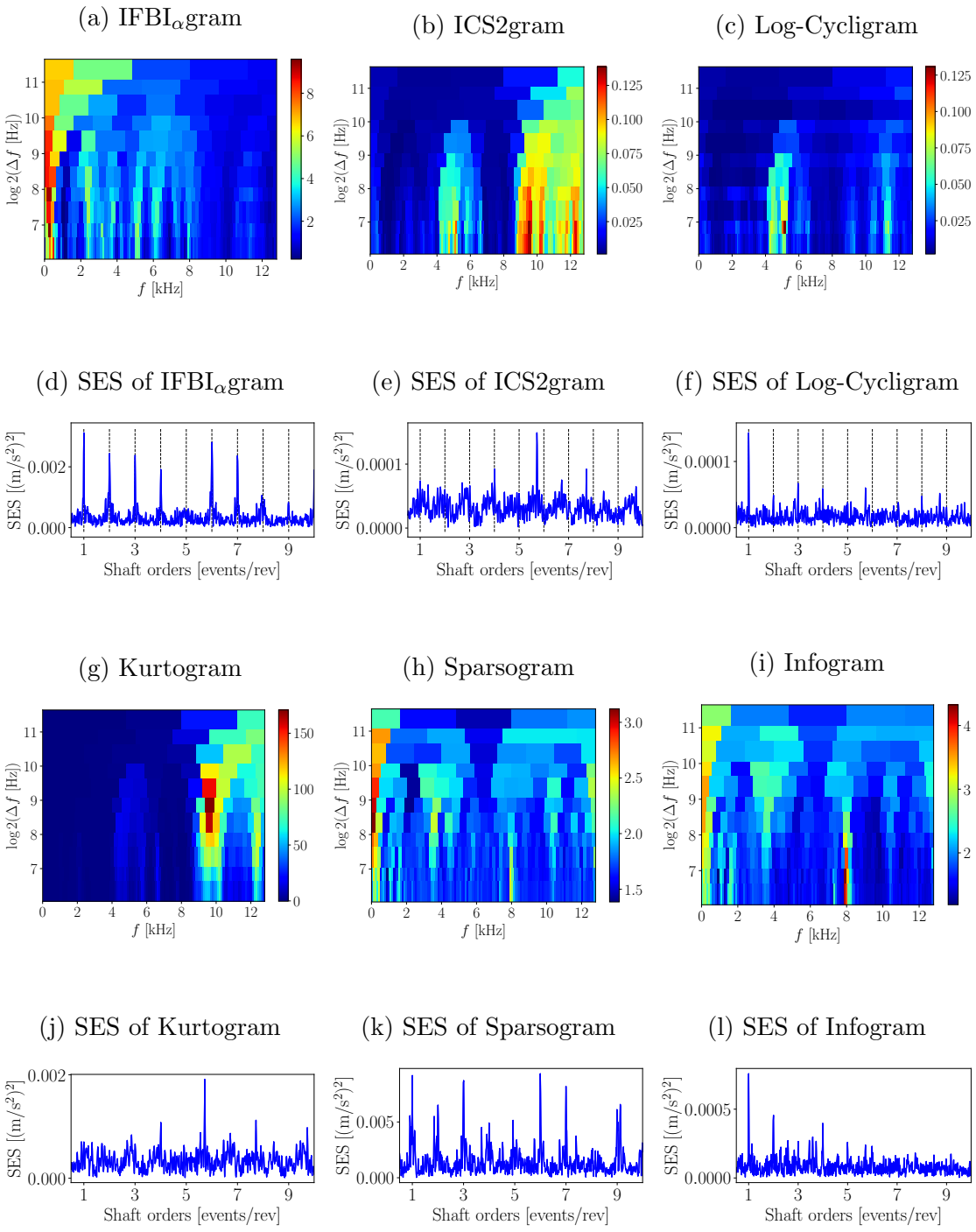

Figure 20: The feature planes and resulting SES of the filtered signals are presented for measurement 1 of the distributed gear damage experiment.

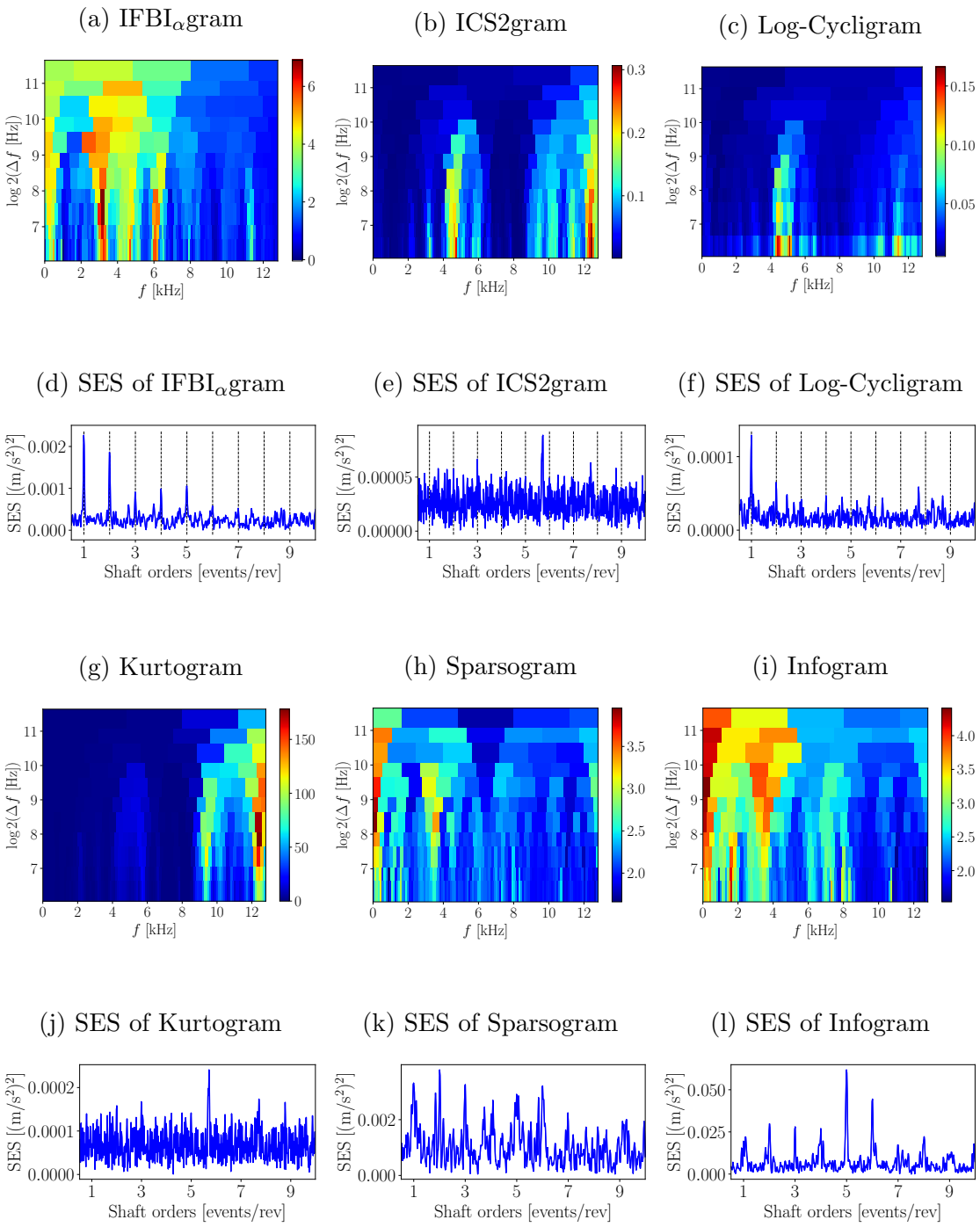

Figure 21: The feature planes and resulting SES of the filtered signals are presented for measurement 2 of the localised gear damage experiment.

age measurements. The log-cycligram performed well in detecting the distributed gear damage for both cases, but could not detect the localised gear damage. This is attributed to the fact that the IFBI$_\alpha$gram uses a signal-to-noise ratio measure (or measure of the prominence of the components-of-interest) to identify informative frequency bands and is more robust to spurious components in the spectral frequency bands.

4.4. Comparison between OFSCoh and OFCMS estimators

The IFBI$_\alpha$gram, originally proposed in Ref. [49], decomposes the vibration signal into a set of Order-Frequency Spectral Coherences (OFSCoh), whereafter the SNR feature given by Equation (19) is calculated to obtain the feature plane. In Section 2, we propose a framework that allows different targeted FBI methods to be applied under time-varying operating conditions by using the OFCMS as an estimator. This makes it possible to compare the performance of the features (e.g. SNR feature vs. Kurtosis feature), since all FBI methods are calculated using the same STFT estimators as basis.

In this section, the original IFBI$_\alpha$gram (i.e. estimated with the OFSCoh [49]) is calculated using the Welch-based estimator of the OFSCoh [55] and presented in Figure 22 for the localised and distributed gear damage measurements considered in this work.

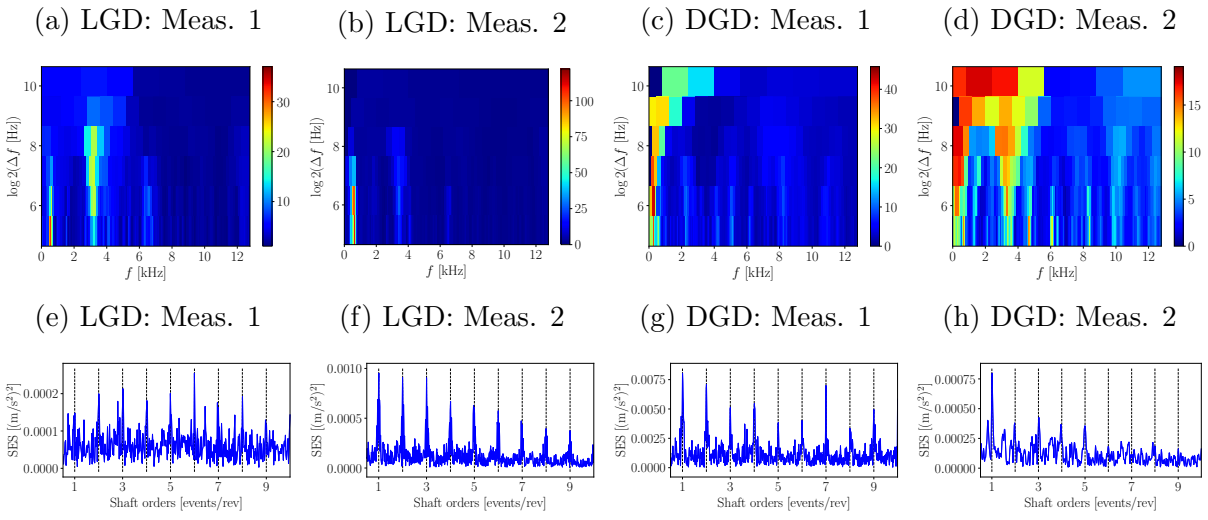

Figure 22: The IFBI$_\alpha$gram, calculated with the OFSCoh, are compared for the different measurements considered in this work.

The gear components (i.e. 1.0 shaft orders and its harmonics) are seen in all measure-

ments. However, the results in Figures 16, 17, 20, 21 and 22 indicate that the OFCMS-based IFBI$_\alpha$gram performs slightly better than the OFSCoh-based IFBI$_\alpha$gram. For example, the gear components are more clearly seen in Figure 16(d) than in Figure 22(e). Furthermore, the performance of the two estimators are quantified in Table 1 and it corroborates the observation that the OFCMS-based IFBI$_\alpha$gram performs slightly better than the OFSCoh-based IFBI$_\alpha$gram on the considered measurements.

Table 1: The performance of the OFCMS-based and OFSCoh-based IFBI$_\alpha$gram is compared for the different considered measurements using the measure in Ref. [27]. A larger feature indicates that the gear component is more prominent. The feature is estimated as follows: The amplitude of a specific harmonic of the gear component (e.g. H1 is the first harmonic) in the SES is divided by the median of the SES in the range $[0, 10]$. The median is calculated as a measure of the noise level.

Meas. name	Estimator	Feat H1	Feat H2	Feat H3
LGD Meas. 1	OFCMS	6.708	7.504	6.708
LGD Meas. 1	OFSCoh	2.711	3.652	2.711
LGD Meas. 2	OFCMS	10.695	10.784	10.695
LGD Meas. 2	OFSCoh	9.618	9.177	9.618
DGD Meas. 1	OFCMS	10.836	7.559	10.836
DGD Meas. 1	OFSCoh	8.202	7.218	8.202
DGD Meas. 2	OFCMS	9.755	7.994	9.755
DGD Meas. 2	OFSCoh	8.202	3.9	8.202

The computational time between the two methods are compared in Table 2 for the different measurements. The results supports the well-known fact that the OFCMS is much more efficient to calculate than the Welch-estimator of the OFSCoh [56]. However, since the OFCMS has a limited cyclic order range (i.e. see Equation (9)) it is not necessarily well-suited for all applications and therefore care needs to be taken when using it to estimate targeted feature planes (e.g. IFBI$_\alpha$gram, ICS2gram).

Table 2: The computational time to construct the OFSCoh-IFBI$_\alpha$gram and OFCMS-IFBI$_\alpha$gram is compared. This was implemented in Python 3.7.3 on a computer with a 32 Gb RAM with an AMD Ryzen 7 2700X Eight-Core processor.

	OFSCoh		OFCMS	
	Meas. 1	Meas. 2	Meas. 1	Meas. 2
LGD	14757.2 [s]	14407.3 [s]	24.8 [s]	23.8 [s]
DGD	12390.5 [s]	15897.8 [s]	25.81 [s]	26.1 [s]

5. Conclusion

In this work, a framework is presented for applying frequency band identification methods under time-varying operating conditions. This framework utilises the instantaneous power spectrum and the cyclic modulation spectrum to estimate blind and targeted features that indicate the frequency bands with potential fault information. Since the same framework is used for all the considered features, it makes it possible to compare the performance of the features under time-varying operating conditions. The results from the two numerical and the two experimental investigations indicate the following:

- Targeted methods perform much better than blind methods for frequency band identification under time-varying operating conditions.
- The performance of the frequency band identification is much dependent on the feature that is used.
- The IFBI$_\alpha$gram, when compared to the established blind and targeted features, has much potential for bearing and gear fault diagnosis under time-varying operating conditions.

Even though targeted methods perform the best, they require the cyclic components to be known a priori, which could be difficult for drive-trains with many cyclic components that need to be monitored. Therefore, there is still much value in obtaining blind methods that perform well and therefore it is necessary to find blind features that are capable of reliably identifying informative frequency bands. Lastly, even though the investigations were performed under varying load and speed conditions; the influence of time-varying

load on the frequency band identification process is not well understood and needs to be investigated in the future.

Acknowledgements

The South African authors gratefully acknowledge the Eskom Power Plant Engineering Institute (EPPEI) for their support in the execution of this research.

Appendix A. Phenomenological gearbox model: Additional information

This model is based on the work by Abboud et al. [23] that was extended to include inner race bearing damage in Ref. [27]. The measured (or casing) vibration signal

$$x_c(t) = x_{gmc}(t) + x_{dgd}(t) + x_{bo}(t) + x_{bi}(t) + x_n(t), \tag{A.1}$$

consists of a gear mesh component $x_{gmc}(t)$, a distributed gear damage component $x_{dgd}(t)$, an outer race bearing damage component $x_{bo}(t)$, an inner race bearing damage component $x_{bi}(t)$ and a broadband noise component $x_n(t)$.

The gear mesh component of the gearbox

$$x_{gmc}(t) = M\left(\omega(t)\right) \cdot h_{gmc}(t) \otimes \left(\sum_{k=1}^{N_{gmc}} A_{gmc}^{(k)} \cdot \sin\left(k \cdot N_{teeth} \cdot \int_0^t \omega(\tau) d\tau + \varphi_{gmc}^{(k)} \right) \right), \tag{A.2}$$

simulates the interaction between healthy gear teeth of a parallel shaft gearbox, where $M\left(\omega(t)\right)$ changes the amplitude of the signal as the rotational speed ω [rad/s] changes, $h_{gmc}(t)$ is the impulse response function of a single degree-of-freedom signal, N_{teeth} is the number of teeth of the gear, which can be used to calculate the instantaneous gear mesh frequency with $N_{teeth} \cdot \omega(t)$. There are N_{gmc} harmonics in the signal with $A_{gmc}^{(i)}$ and $\varphi_{gmc}^{(k)}$ being the amplitude and phase of the kth harmonic. The natural frequency and the damping ratio of $h_{gmc}(t)$ are 2000 Hz and 0.05 respectively.

The distributed gear damage component

$$x_{dgd}(t) = M(\omega(t)) \cdot h_{dgd} \otimes \left(\varepsilon_\sigma(t) \cdot \sum_{k=1}^{N_{dgd}} A_{dgd}^{(k)} \cdot \sin\left(k \cdot \int_0^t \omega(\tau) d\tau + \varphi_{dgd}^{(k)} \right) \right), \tag{A.3}$$

has the same form as the gear mesh signal given by Equation (A.2), except for the addition of $\varepsilon_\sigma(t)$. The function $\varepsilon_\sigma(t)$ is a sample from a standardised Gaussian, which makes the

distributed gear damage component random as opposed to gear mesh component which is deterministic. The natural frequency and the damping ratio of $h_{gmc}(t)$ are 1300 Hz and 0.05 respectively.

The outer race bearing damage component

$$x_{bo}(t) = M(\omega(t)) \cdot h_{bo}(t) \otimes \left(\sum_{k=0}^{N_{imp}-1} A_{bo}^{(k)} \cdot \delta\left(t - T_{bo}^{(k)}\right) \right), \tag{A.4}$$

comprises of a train of impulses, where the kth impulse $\delta\left(t - T_{bo}^{(k)}\right)$ occurs at the time where $t = T_{bo}^{(k)}$ and has an amplitude of $A_{bo}^{(k)}$. The $T_{bo}^{(k)}$ is dependent on the rotational speed of the system as well as on slip. However, the signal is simulated in the time domain to retain the angle-time cyclostationary properties of the signal [57]. The impulse is ultimately filtered through the structure which is assumed to have an impulse response function $h_{bo}(t)$ of a single degree-of-freedom system with a natural frequency and damping ratio of 7000 Hz and 0.05 respectively.

The inner race damage component

$$x_{bi}(t) = z_{stribeck}\left(\int_0^t \omega(\tau)d\tau\right) \cdot M(\omega(t)) \cdot h_{bi} \otimes \left(\sum_{k=0}^{N_{imp}-1} A_{bi}^{(k)} \cdot \delta\left(t - T_{bi}^{(k)}\right) \right), \tag{A.5}$$

has a similar form as the outer race bearing damage component, however, there is additional modulation simulated with $z_{stribeck}\left(\int_0^t \omega(\tau)d\tau\right)$ as the bearing damage moves in-and-through the load zone. This phenomenon is simulated with the Stribeck equation [5]

$$z_{stribeck}(\varphi) = \begin{cases} z_0 \cdot \left(1 - \frac{1}{2\epsilon}\left(1 - \cos(\varphi)\right)\right)^{c_{str}} & \text{for } |\text{wrp}(\varphi)| < \varphi_{max} \\ 0 & \text{otherwise,} \end{cases} \tag{A.6}$$

The wrap function, denoted by $\text{wrp}(\varphi)$, returns the phase of the shaft φ in the domain of $[-\pi,\ \pi]$. The constants associated with the Stribeck equation is as follows in this work [5]: $c_{str} = 3/2$, $\epsilon = 0.49$, $\varphi_{max} = 0.99\pi/2\text{rad}$, and $z_0 = 1$. The natural frequency and the damping ratio of $h_{bi}(t)$ are 5500 Hz and 0.05 respectively.

The broadband noise component in the signal

$$x_n(t) = \sigma_n \cdot \varepsilon_\sigma(t) \cdot M(\omega(t)), \tag{A.7}$$

Table A.3: Different statistics of the signal components of the model are presented. The SNR of signal x_i is calculated with $10 \cdot \log_{10}(E_i/E_n)$, where E_i is the energy of x_i and E_n is the energy of the noise component.

	x_{gmc}	x_{dgd}	x_{bi}	x_{bo}
SNR	2.91	1.01	-17.75	-17.75
Max.	1210.95	2526.24	829.97	535.9
RMS	347.65	279.12	32.21	32.21

is simulated by drawing samples from a standardized Gaussian $\varepsilon_\sigma(t)$ and scaling them with a factor σ_n and the rotational speed of the system $M(\omega(t))$. The scaling of the amplitude due to the rotational speed is simulated by $M(\omega(t)) = \omega^2$.

The signal-to-noise ratio, the maximum value and the RMS of the different signal components are given in Table A.3. The distributed gear damage is clearly much more dominant than the bearing damage components.

References

[1] A. K. S. Jardine, D. Lin, D. Banjevic, A review on machinery diagnostics and prognostics implementing condition-based maintenance, Mechanical Systems and Signal Processing 20 (7) (2006) 1483–1510.

[2] H. M. Hashemian, S. Member, State-of-the-Art Predictive Maintenance Techniques, IEEE Transactions on Instrumentation and Measurement 60 (1) (2011) 226–236.

[3] X. Wang, V. Makis, Autoregressive model-based gear shaft fault diagnosis using the Kolmogorov-Smirnov test, Journal of Sound and Vibration 327 (3-5) (2009) 413–423.

[4] S. Baudin, D. Rémond, J. Antoni, O. Sauvage, Non-intrusive rattle noise detection in non-stationary conditions by an angle/time cyclostationary approach, Journal of Sound and Vibration 366 (2016) 501–513.

[5] P. D. McFadden, J. D. Smith, Vibration monitoring of rolling element bearings by the high-frequency resonance technique - a review, Tribology International 17 (1) (1984) 3–10.

[6] M. Buzzoni, J. Antoni, G. D. Elia, Blind deconvolution based on cyclostationarity maximization and its application to fault identification, Journal of Sound and Vibration 432 (2018) 569–601.

[7] P. D. Samuel, D. J. Pines, A review of vibration-based techniques for helicopter transmission diagnostics, Journal of Sound and Vibration 282 (1-2) (2005) 475–508.

[8] A. Mauricio, L. Zhou, D. Mba, K. Gryllias, Vibration based condition monitoring of helicopter gearboxes based on cyclostationary analysis, Journal of Engineering for Gas Turbines and Power (Accepted).
URL https://doi.org/10.1115/1.4044453

[9] W. Bartelmus, R. Zimroz, A new feature for monitoring the condition of gearboxes in non-stationary operating conditions, Mechanical Systems and Signal Processing 23 (5) (2009) 1528–1534.

[10] R. Zimroz, W. Bartelmus, T. Barszcz, J. Urbanek, Diagnostics of bearings in presence of strong operating conditions non-stationarity - A procedure of load-dependent features processing with application to wind turbine bearings, Mechanical Systems and Signal Processing 46 (1) (2014) 16–27.

[11] T. Barszcz, R. B. Randall, Application of spectral kurtosis for detection of a tooth crack in the planetary gear of a wind turbine, Mechanical Systems and Signal Processing 23 (4) (2009) 1352–1365.

[12] J. Urbanek, T. Barszcz, R. Zimroz, J. Antoni, Application of averaged instantaneous power spectrum for diagnostics of machinery operating under non-stationary operational conditions, Measurement 45 (7) (2012) 1782–1791.

[13] A. Mauricio, S. Sheng, K. Gryllias, Condition monitoring of wind turbine planetary gearboxes under different operating conditions, Journal of Engineering for Gas Turbines and Power (Accepted).
URL https://doi.org/10.1115/1.4044683

[14] J. P. Salameh, S. Cauet, E. Etien, A. Sakout, L. Rambault, Gearbox condition monitoring in wind turbines: A review, Mechanical Systems and Signal Processing 111 (2018) 251–264.

[15] A. Stetco, F. Dinmohammadi, X. Zhao, V. Robu, D. Flynn, M. Barnes, J. Keane, G. Nenadic, Machine learning methods for wind turbine condition monitoring: A review, Renewable energy 133 (2019) 620–635.

[16] Y. Lei, B. Yang, X. Jiang, F. Jia, N. Li, A. K. Nandi, Applications of machine learning to machine fault diagnosis: A review and roadmap, Mechanical Systems and Signal Processing 138 (2020) 106587.

[17] F. Jia, Y. Lei, J. Lin, X. Zhou, N. Lu, Deep neural networks: A promising tool for fault characteristic mining and intelligent diagnosis of rotating machinery with massive data, Mechanical Systems and Signal Processing 72 (2016) 303–315.

[18] S. Khan, T. Yairi, A review on the application of deep learning in system health management, Mechanical Systems and Signal Processing 107 (2018) 241–265.

[19] R. Zhao, R. Yan, Z. Chen, K. Mao, P. Wang, R. X. Gao, Deep learning and its applications to machine health monitoring, Mechanical Systems and Signal Processing 115 (2019) 213–237.

[20] R. B. Randall, J. Antoni, Rolling element bearing diagnosticsa tutorial, Mechanical systems and signal processing 25 (2) (2011) 485–520.

[21] J. Antoni, Cyclostationarity by examples, Mechanical Systems and Signal Processing 23 (4) (2009) 987–1036.

[22] D. Abboud, J. Antoni, S. Sieg-Zieba, M. Eltabach, Deterministic-random separation in nonstationary regime, Journal of Sound and Vibration 362 (2016) 305–326.

[23] D. Abboud, J. Antoni, S. Sieg-Zieba, M. Eltabach, Envelope analysis of rotating machine vibrations in variable speed conditions: A comprehensive treatment, Mechanical Systems and Signal Processing 84 (2017) 200–226.

[24] P. Borghesani, P. Pennacchi, R. B. Randall, N. Sawalhi, R. Ricci, Application of cepstrum pre-whitening for the diagnosis of bearing faults under variable speed conditions, Mechanical Systems and Signal Processing 36 (2) (2013) 370–384.

[25] G. Yu, C. Li, J. Zhang, A new statistical modeling and detection method for rolling element bearing faults based on alpha-stable distribution, Mechanical Systems and Signal Processing 41 (1-2) (2013) 155–175.

[26] C. J. Stander, P. S. Heyns, W. Schoombie, Using vibration monitoring for local fault detection on gears operating under fluctuating load conditions, Mechanical Systems and Signal Processing 16 (6) (2002) 1005–1024.

[27] S. Schmidt, P. S. Heyns, K. C. Gryllias, A pre-processing methodology to enhance novel information for rotating machine diagnostics, Mechanical Systems and Signal Processing 124 (2019) 541–561.

[28] X. Y. Wang, V. Makis, M. Yang, A wavelet approach to fault diagnosis of a gearbox under varying load conditions, Journal of Sound and Vibration 329 (9) (2010) 1570–1585.

[29] Z. Feng, M. Liang, F. Chu, Recent advances in time–frequency analysis methods for machinery fault diagnosis: A review with application examples, Mechanical Systems and Signal Processing 38 (1) (2013) 165–205.

[30] R. Yan, R. X. Gao, X. Chen, Wavelets for fault diagnosis of rotary machines: A review with applications, Signal processing 96 (2014) 1–15.

[31] L. Xiao, X. Zhang, S. Lu, T. Xia, L. Xi, A novel weak-fault detection technique for rolling element bearing based on vibrational resonance, Journal of Sound and Vibration 438 (2019) 490–505.

[32] Z. Li, X. Liu, X. Wang, T. He, Y. Shan, A multi-parameter constrained potential underdamped stochastic resonance method and its application for weak fault diagnosis, Journal of Sound and Vibration 459 (2019) 114862.

[33] J. Antoni, The spectral kurtosis: A useful tool for characterising non-stationary signals, Mechanical Systems and Signal Processing 20 (2) (2006) 282–307.

[34] Y. Cheng, B. Chen, G. Mei, Z. Wang, W. Zhang, A novel blind deconvolution method and its application to fault identification, Journal of Sound and Vibration 460 (2019) 114900.

[35] J. Antoni, Fast computation of the kurtogram for the detection of transient faults, Mechanical Systems and Signal Processing 21 (1) (2007) 108–124.

[36] W. A. Smith, P. Borghesani, Q. Ni, K. Wang, Z. Peng, Optimal demodulation-band selection for envelope-based diagnostics: A comparative study of traditional and novel tools, Mechanical Systems and Signal Processing 134 (2019) 106303.

[37] T. Barszcz, A. Jabłoński, A novel method for the optimal band selection for vibration signal demodulation and comparison with the Kurtogram, Mechanical Systems and Signal Processing 25 (1) (2011) 431–451.

[38] J. Hebda-Sobkowicz, R. Zimroz, A. Wyłomańska, Selection of the informative frequency band in a bearing fault diagnosis in the presence of non-gaussian noisecomparison of recently developed methods, Applied Sciences 10 (8) (2020) 2657.

[39] J. Antoni, R. B. Randall, The spectral kurtosis: Application to the vibratory surveillance and diagnostics of rotating machines, Mechanical Systems and Signal Processing 20 (2) (2006) 308–331.

[40] Y. Lei, J. Lin, Z. He, Y. Zi, Application of an improved kurtogram method for fault diagnosis of rolling element bearings, Mechanical Systems and Signal Processing 25 (5) (2011) 1738–1749.

[41] S. Wang, J. Yub, E. Lapirac, J. Lee, A modified support vector data description based novelty detection approach for machinery components, Applied Soft Computing Journal 13 (2) (2013) 1193–1205.

[42] W. A. Smith, Z. Fan, Z. Peng, H. Li, R. B. Randall, Optimised Spectral Kurtosis

for bearing diagnostics under electromagnetic interference, Mechanical Systems and Signal Processing 75 (2015) 371–394.

[43] P. W. Tse, D. Wang, The design of a new sparsogram for fast bearing fault diagnosis: Part 1 of the two related manuscripts that have a joint title as "two automatic vibration-based fault diagnostic methods using the novel sparsity measurement - Parts 1 and 2", Mechanical Systems and Signal Processing 40 (2) (2013) 499–519.

[44] J. Antoni, The infogram: Entropic evidence of the signature of repetitive transients, Mechanical Systems and Signal Processing 74 (2016) 73–94.

[45] D. Wang, An extension of the infograms to novel Bayesian inference for bearing fault feature identification, Mechanical Systems and Signal Processing 80 (2016) 19–30.

[46] A. Moshrefzadeh, A. Fasana, The Autogram: An effective approach for selecting the optimal demodulation band in rolling element bearings diagnosis, Mechanical Systems and Signal Processing 105 (2018) 294–318.

[47] A. Mauricio, J. Qi, W. A. Smith, M. Sarazin, R. B. Randall, K. Janssens, K. Gryllias, Bearing diagnostics under strong electromagnetic interference based on integrated spectral coherence, Mechanical Systems and Signal Processing 140 (2020) 106673.

[48] A. Mauricio, W. A. Smith, R. B. Randall, J. Antoni, K. Gryllias, Improved envelope spectrum via feature optimisation-gram (iesfogram): A novel tool for rolling element bearing diagnostics under non-stationary operating conditions, Mechanical Systems and Signal Processing 144 (2020) 106891.

[49] S. Schmidt, A. Mauricio, P. S. Heyns, K. C. Gryllias, A methodology for identifying information rich frequency bands for diagnostics of mechanical components-of-interest under time-varying operating conditions, Mechanical Systems and Signal Processing 142 (2020) 106739.

[50] Q. Ni, K. Wang, J. Zheng, Rolling Element Bearings Fault Diagnosis Based on a Novel Optimal Frequency Band Selection Scheme, IEEE Access 7 (2019) 80748–80766.

[51] Z. Liu, Y. Jin, M. J. Zuo, D. Peng, Accugram: A novel approach based on classification to frequency band selection for rotating machinery fault diagnosis, ISA transactions 95 (2019) 346–357.

[52] T. Wang, Q. Han, F. Chu, Z. Feng, A new skrgram based demodulation technique for planet bearing fault detection, Journal of Sound and Vibration 385 (2016) 330–349.

[53] T. Wang, F. Chu, Q. Han, Y. Kong, Compound faults detection in gearbox via meshing resonance and spectral kurtosis methods, Journal of Sound and Vibration 392 (2017) 367–381.

[54] W. N. Niehaus, S. Schmidt, P. S. Heyns, Nic methodology: A probabilistic methodology for improved informative frequency band identification by utilizing the available healthy historical data under time-varying operating conditions, Journal of Sound and Vibration 488 (2020) 115642.

[55] D. Abboud, S. Baudin, J. Antoni, D. Rémond, M. Eltabach, O. Sauvage, The spectral analysis of cyclo-non-stationary signals, Mechanical Systems and Signal Processing 75 (2016) 280–300.

[56] D. Abboud, J. Antoni, Order-frequency analysis of machine signals, Mechanical Systems and Signal Processing 87 (October 2016) (2017) 229–258.

[57] D. Abboud, J. Antoni, M. Eltabach, S. Sieg-zieba, Angle\time cyclostationarity for the analysis of rolling element bearing vibrations, Measurement 75 (2015) 29–39.

[58] S. Baudin, D. Rémond, J. Antoni, O. Sauvage, Non-intrusive rattle noise detection in non-stationary conditions by an angle/time cyclostationary approach, Journal of Sound and Vibration 366 (2016) 501–513.

[59] S. Schmidt, A. Mauricio, P. S. Heyns, K. C. Gryllias, A new method for identifying diagnostic rich frequency bands under varying operating conditions, Surveillance, Vishno and AVE conferences, INSA-Lyon, Universite de Lyon, July 2019, Lyon, France.
URL https://hal.archives-ouvertes.fr/hal-02188569/

[60] P. Borghesani, P. Pennacchi, S. Chatterton, The relationship between kurtosis-and envelope-based indexes for the diagnostic of rolling element bearings, Mechanical Systems and Signal Processing 43 (1-2) (2014) 25–43.

[61] X. Xu, M. Zhao, J. Lin, Y. Lei, Envelope harmonic-to-noise ratio for periodic impulses detection and its application to bearing diagnosis, Measurement 91 (2016) 385–397.

[62] D. Wang, Spectral l2/l1 norm: A new perspective for spectral kurtosis for characterizing non-stationary signals, Mechanical Systems and Signal Processing 104 (2018) 290–293.

[63] J. Obuchowski, A. Wylomanska, R. Zimroz, Selection of informative frequency band in local damage detection in rotating machinery, Mechanical Systems and Signal Processing 48 (1-2) (2014) 138–152.

[64] J. Hebda-Sobkowicz, R. Zimroz, M. Pitera, A. Wyłomańska, Informative frequency band selection in the presence of non-gaussian noise–a novel approach based on the conditional variance statistic with application to bearing fault diagnosis, Mechanical Systems and Signal Processing 145 (2020) 106971.

[65] J. Antoni, D. Hanson, Detection of surface ships from interception of cyclostationary signature with the cyclic modulation coherence, IEEE Journal of Oceanic Engineering 37 (3) (2012) 478–493.

[66] J. Antoni, G. Xin, N. Hamzaoui, Fast computation of the spectral correlation, Mechanical Systems and Signal Processing 92 (2017) 248–277.

[67] P. Borghesani, J. Antoni, A faster algorithm for the calculation of the fast spectral correlation, Mechanical Systems and Signal Processing 111 (2018) 113–118.

[68] K. Fyfe, E. Munck, Analysis of computed order tracking, Mechanical Systems and Signal Processing 11 (2) (1997) 187–205.

[69] S. Schmidt, P. Heyns, J. de Villiers, A tacholess order tracking methodology based on a probabilistic approach to incorporate angular acceleration information into the

maxima tracking process, Mechanical Systems and Signal Processing 100 (2018) 630–646.

[70] D. Wang, P. W. Tse, K. L. Tsui, An enhanced Kurtogram method for fault diagnosis of rolling element bearings, Mechanical Systems and Signal Processing 35 (1-2) (2013) 176–199.

[71] D. Wang, Z. Peng, L. Xi, The sum of weighted normalized square envelope: A unified framework for kurtosis, negative entropy, gini index and smoothness index for machine health monitoring, Mechanical Systems and Signal Processing 140 (2020) 106725.

[72] A. Raad, J. Antoni, M. Sidahmed, Indicators of cyclostationarity: Theory and application to gear fault monitoring, Mechanical Systems and Signal Processing 22 (3) (2008) 574–587.

[73] K. Feng, W. A. Smith, P. Borghesani, R. B. Randall, Z. Peng, Use of cyclostationary properties of vibration signals to identify gear wear mechanisms and track wear evolution, Mechanical Systems and Signal Processing 150 107258.

[74] I. El-Thalji, E. Jantunen, A summary of fault modelling and predictive health monitoring of rolling element bearings, Mechanical systems and signal processing 60 (2015) 252–272.

[75] M. Cerrada, R.-V. Sánchez, C. Li, F. Pacheco, D. Cabrera, J. V. de Oliveira, R. E. Vásquez, A review on data-driven fault severity assessment in rolling bearings, Mechanical Systems and Signal Processing 99 (2018) 169–196.

[76] F. Chaari, W. Bartelmus, R. Zimroz, T. Fakhfakh, M. Haddar, Gearbox vibration signal amplitude and frequency modulation, Shock and Vibration 19 (4) (2012) 635–652.